ISOTOPIC EFFECTS IN H_2^+ DYNAMICS

IN AN INTENSE LASER FIELD

by

JIANJUN HUA

A THESIS

submitted in partial fulfillment of the

requirements for the degree

MASTER of SCIENCE

Department of Physics

College of Arts and Sciences

KANSAS STATE UNIVERSITY

Manhattan, Kansas

2009

Approved by:

Major Professor

Brett D. Esry

Copyright

Jianjun Hua

2009

This document is presented using LaTeX

Abstract

The two-state field-aligned (1-D) model has been employed to investigate the dissociation dynamics of a hydrogen molecular ion and its isotopes under the Born-Oppenheimer approximation without rotation. The emphasis of this work was on the role of mass during the dynamical dissociation processes and on the laser-induced branching ratios between different photon pathways.

Firstly, we have found that scaling the pulse duration of the laser pulse, applied to H_2^+ and D_2^+, by the square root of the mass ratio of these isotopes will produce similar structure in the nuclear kinetic energy release (KER) spectra. In fact, the similarity of the spectra is enhanced by including some averaging that is necessary for comparison with experiment. For this to occur, the same broad initial vibrational distribution and a short pulse are preferred. Using this scaling idea, it is possible to produce effectively shorter laser pulses by studying heavier isotopes, like D_2^+.

Secondly, we have demonstrated analytically and numerically that there is a carrier-envelope phase effect in the total dissociation probability (TDP) of H_2^+, and this effect grows with nuclear mass. We further show that under the same laser conditions, the CEP effect in the asymmetry between breakup channels decreases with mass. Our analytic expressions enhance the idea that CEP effects can be understood as an interference between different n-photon processes.

Thirdly, the trends in the dissociation dynamics of H_2^+ and D_2^+ in a 800nm ultrashort intense laser field were demonstrated by studying the dissociation branching ratios of multiphoton processes as a function of the laser peak intensity (from 8×10^9 to 10^{14} W/cm^2) or pulse length (5fs-7.5fs). Based on the two-state approximation, an energy-analysis method

(EAM) was employed to separate multiphoton processes. The results show that the one-photon dissociation process dominates over all other photon processes under all the laser conditions applied in the calculations and that the zero-photon process contributes to a surprisingly large fraction of the total dissociation. Two- and three- photon dissociation are weaker processes, but become more and more important as the laser peak intensity and pulse length increases. A two-state Floquet method was used to check the accuracy of the EAM, and good agreement between the two methods was found, demonstrating the reliability of the EAM. In comparison with H_2^+, D_2^+ displays stronger two and three photon branching ratios (above-threshold dissociation — ATD), which can be attributed to the late arrival of D_2^+ to the critical distance for ATD to occur due to its heavier mass. Therefore, this "mass" effect can be used to steer the molecular dissociation pathways.

Contents

List of Figures

List of Tables

Acknowledgments

I would like to express my appreciation and acknowledgement to the following people because without their help, support, guidance and efforts, it is hard to accomplish what I have reached today. First, I would like to thank my major advisor Dr. Brett D. Esry as his patience, and encouragement have driven me through my graduate career at Kansas State University and the knowledge I have learned from him will benefit my future career. I would also like to thank Dr. Itzik Ben-Itzhak for his advice and help and Dr.Chii-Dong Lin for his understanding and advice. Thanks also go to Dr. Kevin Carnes for proofreading papers I drafted and reminding me to further improve my English. I am thankful to have worked with the research associate, Dr. Jarlath McKenna, who possesses excellent research abilities and wonderful personal characters. I also acknowledge that I am very lucky to work with these excellent graduate students: Fatima Anis, A. Max Sayler, Yujun Wang, Bishwanath Gaire, Nora G. Johnson, Mohammad Zohrabi, who make my day-to-day work full of fun.

On a personal note, I wish to thank my wife, Yi Xiao, whose ever-lasting love and support have tided me over the ups and downs in my life. I would also like to thank our parents and my sister for their endless love and support. Special thanks go to my Chinese and American friends for their understanding and support.

Chapter 1

Introduction

1.1 First Brick: H_2^+ and Laser

Due to the simplest molecular structure in nature, the single-electron diatomic molecules, H_2^+ and its isotopes (D_2^+, T_2^+, HD^+), especially D_2^+, have drawn a great deal of attention over the past two decades. In this time, substantial progress has been made (see, for instance, the reviews in [1, 2]). This system serves as a starting point to test new theoretical models or new experimental phenomena and as a benchmark that has already given us insight into the response of more complicated molecules to ultrashort intense laser fields. Recently, experiments on H_2^+ and D_2^+ molecular beams have also been carried out, making direct comparison between theory and experiment possible [3–6].

On the other hand, the booming development of intense laser technology has been a strong boost for the study of molecular dynamics. Nowadays, the production of a femtosecond laser pulse, whose duration can be on the same time scale as the nuclear vibrational motion and whose field strength can be comparable to the internal force fields binding electrons to molecules, has become a routine technique. Meanwhile, researchers have been trying to gain optimal controls over the dynamics of atomic or molecular systems by manipulating the laser, such as its peak intensity [7–10], pulse length [8, 9, 11, 12], pulse shape [7, 13],

wavelength [1, 2, 7, 14, 15], or carrier-envelope phase [16–26]. Also, more than one laser pulse can be used in that process, for example, in pump-probe experiments where a pair of laser pulses are used [27], or even a train of laser pulses can be employed [28].

In this thesis, the strong-field behavior associated with the one-electron diatomic homonuclear systems, H_2^+, and its isotopes, D_2^+ and T_2^+, is investigated. Taking H_2^+ as an example, when this molecule is illuminated by an intense laser field, it will either dissociate,

$$H_2^+ + n\hbar\omega \rightarrow p + H(nl) \tag{1.1}$$

or ionize,

$$H_2^+ + m\hbar\omega \rightarrow p + p + e^-. \tag{1.2}$$

This thesis is focused on the dissociation mechanism (1.1), which dominates at intensities less than about 10^{14} Wcm^{-2}.

Apart from the laser per se, it is possible to achieve control from the other factor involved in the interaction: the atomic or molecular system itself. In other words, under the same laser conditions, the properties of the atomic or molecular system can also be used to get, or infer, the expected results. Among others, mass can be easily employed to realize the goal. Sometimes mass plays quite an important role in a dynamical process, such as in isotopic effects. More recently, it has been shown that the nuclear mass can be used to help enable control of the electrons as well [29]. It has also been shown that mass can enhance carrier-envelope phase effects [18] and above threshold dissociation [9].

1.2 Focus of this Thesis

The mass role in the dissociation of H_2^+ in an ultrashort intense laser field (Chapter 4 and Chapter 5) and branching ratios of different photon processes (Chapter 6) are the two major aspects of this thesis. To be specific, a H_2^+ molecular ion irradiated by an ultrashort intense

laser pulse in the infrared absorption wavelength regime (800nm) is taken as an illustrative example in the thesis. By the comparison of different hydrogenic isotopes, we try to trace out the trends of the role of mass in the dynamical process and laser parameter dependencies of the dynamics of the dissociation.

Relevant experimental techniques and procedures will be briefly stated in Chapter 2. The theoretical models and relevant concepts used in this thesis will be interpreted in Chapter 3. The main conclusions for the thesis will be drawn in Chapter 7.

Atomic units are used throughout this thesis unless otherwise specified.

Chapter 2

Experimental Background

2.1 Experimental Tools

There are different experimental setups, which mainly consist of a laser system and ion beam, that are designed to investigate the dynamics of H_2^+ in an intense laser field. The laser system is capable of producing intensities in the range of $10^{10} - 10^{16}$ Wcm^{-2} which is focused into an ultra-high vacuum system equipped with energy-resolved ion mass and/or photoelectron spectrometers. The laser and ion beams are crossed in a reaction region and fragments are separated by an electromagnetic field. The fragments are captured and recorded as signals by electronics.

2.2 Laser Technology

First of all, let us discuss a laser system. In the past two decades, researchers were not satisfied with CW lasers or "long" picosecond pulsed lasers. The higher requirement for the understanding of the dynamics of small molecules in intense laser fields has pushed forward the technology of ultra-short pulsed lasers to progress to such an extent that femtosecond lasers are now routine tools in a laboratory. Recently, this momentum has even furthered

the technology to the attosecond kingdom, where it is hoped that the dynamics of electrons can be finally resolved.

2.2.1 Ti:Sapphire Laser

To make an intense laser field in the laboratory it is necessary to have a laser that delivers an appreciable amount of energy in a sufficiently short pulse. In the intense-field regime the most versatile laser system is probably the femtosecond titanium sapphire laser ($Ti:Al_2O_3$), which consists of two principle components, the oscillator and the amplifier. The material Ti:sapphire has the largest gain bandwidth (235 nm FWHM) [2] compared with other commonly used laser media, therefore, it enables a very broad frequency spectrum yielding a very short pulse. Moreover, it is a table-top system, meaning that the whole laser system fits on one optical table. The systems are completely 'solid state', which render them user friendly.

2.2.2 Pulse Length Measurement

A pulsed laser can be mainly characterized by its wavelength, pulse length (pulse duration), peak intensity and carrier-envelope phase. Among others, the latter three are the parameters that are most often measured and manipulated in a lab.

In the past, autocorrelation techniques were used to estimate the pulse length of a ultrashort pulses. However, if pulse lengths are smaller than 50fs, autocorrelation is usually unsatisfactory because the broad bandwidth of the pulses gives rise to problems due to phase matching in the doubling crystals used to produce the pulses. For a-few-cycle-long pulse, the pulse shape becomes important. In the past decade, the most commonly used tools to characterize ultrashort pulsed lasers are frequency-resolved optical gating (FROG) [2, 30–32] and spectral phase interferometry for direct electric-field reconstruction (SPIDER) [33–35].

FROG is an autocorrelation technique for the characterization of optical pulses in which the frequencies in the second harmonic pulse are resolved with a spectrometer. FROG is

based on the idea that a short pulse can be used to obtain a sample from a longer pulse by nonlinear mixing in a nonlinear crystal material. Pulse shape can be retrieved using an iterative algorithm, i.e. FROG actually uses the pulse itself for gating. This makes the method simple to apply.

Different from FROG, SPIDER is a single shot technique and works with a non-iterative algorithm capable of operating at tens of Hz, which makes real-time measurements practical. The input pulse is divided by a beam splitter into two replicas: one passes through a Michelson interferometer, while the other goes through another arm and is stretched (chirped). After recombination of the two beams, the two short pulses overlap with different frequency components of the chirped pulse. The interaction of the two beams in the doubling crystal produces two pulses with identical shape but different frequency shifted relative to each other. The optical spectrum of the sum frequency signal reveals the temporally resolved group delay. From the group delay, it is easy to retrieve the frequency-dependent spectral phase, so that pulse characterization is achieved.

2.2.3 Focal Volume Effect $\Longrightarrow$ Intensity Averaging

The high non-linearity of intense laser-molecule interactions makes it difficult to resolve the dynamics due to spatial inhomogeneity of the laser intensity. It is because the molecular beam overlaps not only with the center of the laser focus, but also with surrounding shells where the laser intensity is lower [2]. So, to compare with experimental results, the focal volume of the laser must be considered. In Sec. 3.1.3, we refer to this process as *intensity averaging* and a detailed explanation will be given there.

2.2.4 Carrier-Envelope Phase (CEP)

The carrier-envelope phase (CEP) (or absolute phase) of a laser pulse is defined as the difference between the phase of the carrier wave and the envelope (see Fig. 2.1). With the fast development of technologies for producing ever shorter pulses, CEP effects in intense
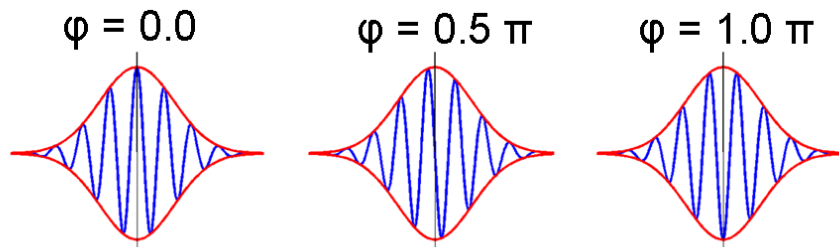
Figure 2.1: Carrier-Envelope Phase

laser field-matter interactions have become more and more important. The corresponding theoretical analysis and experimental measurements for the absolute phase have started [17, 36–38]. Recent experiments have confirmed that CEP can be determined by use of its sensitivity on above-threshold ionization (ATI) [17] or high-harmonic generation (HHG) [39].

Due to pulse energy fluctuations and optical non-linearities in the cavity where the pulse is produced, the CEP usually is not fixed but changed from one pulse to another. The "f-to-2f" interferometry has been adopted to stabilize and lock the pulse-to-pulse shift in the phase [40–44]. However, the disadvantage of the "f-to-2f" interferometer is that it is not a reliable tool to measure the absolute value of the CEP, but only suitable for controlling the pulse-to-pulse shift. The use of the sensitivity of multi-photon-induced photoelectron emission from a metal surface to the CEP has recently been proposed to avoid this limitation [45]. Unlike "f-to-2f" interferometric technique, this technique, combined with standard pulse (envelope) diagnostic systems, is capable of precisely measuring and controlling the electromagnetic field evolution of an ultrashort laser pulses since it can measure the carrier-envelope phase directly [46].

2.3   H$_2$ vs H$_2^+$

There are a few advantages to the use of a H$_2^+$ molecular ion beam as a target rather than by producing H$_2^+$ via ionization of H$_2$ with the same laser pulse. These are as follows:

(1) no rescattering electron is produced in an ion beam, so it makes the interpretation of the experimental results easier than in a neutral H_2 target; (2) the dissociation of H_2^+ can be studied at intensities lower than the appearance intensity for the single ionization of a H_2 molecule, and (3) in the H_2^+ beam, higher vibrational states of H_2^+ are significantly populated (an incoherent Franck-Condon distribution) than the ones in H_2^+ produced from H_2 beam [47]. However, there are also some disadvantages: (1) the density of an ion target is typically many orders of magnitude smaller than that of a neutral target, which makes it much harder to collect statistically adequate data; (2) for an ion target, the measurement of the photoelectrons is still an unresolved experimental problem due to the large number of photoelectrons in the residual gas [48]. Thank to these significant differences, neutral and ion beam target can serve as complementary methods for understanding the different dynamical processes caused by the interaction between molecules and intense laser. Profs. Figger and Hänsch's group [5, 6] initiated the studies of the interaction of intense lasers with H_2^+ beams and soon afterwards followed by Prof. Williams' group [4] and then Prof. Ben-Itzhak's group [3]

2.4   3D Coincidence Setup

Since the theory we have done is in collaboration with Prof. Ben-Itzhak's group, this section is used to briefly state their experimental setup. The setup used is a coincidence 3D momentum imaging setup. A brief introduction to that setup is given in [3, 47, 48] and below. In the setup, the H_2^+ beam is created by electron impact ionization from H_2 in an electron cyclotron resonance (ECR) ion source. This ionization process gives rise to an approximate Franck-Condon distribution, which is produced by a vertical transition, of the vibrational states in H_2^+ ground electronic state ($1s\sigma_g$). The ion beam is accelerated by an electric field and steered and collimated into the reaction region, where the ion beam is crossed with a 790nm Ti:sapphire laser beam at roughly 90°. The charged fragments produced by
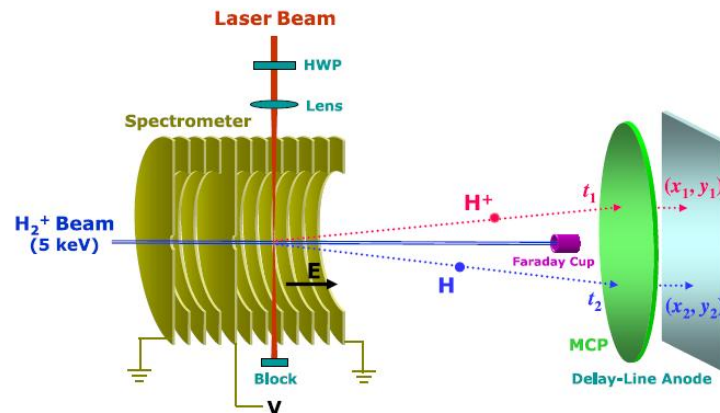
Figure 2.2: Schematic view of the experimental setup. HWP: half wave plate, MCP: microchannel plate. (Figure reproduced from [48]).
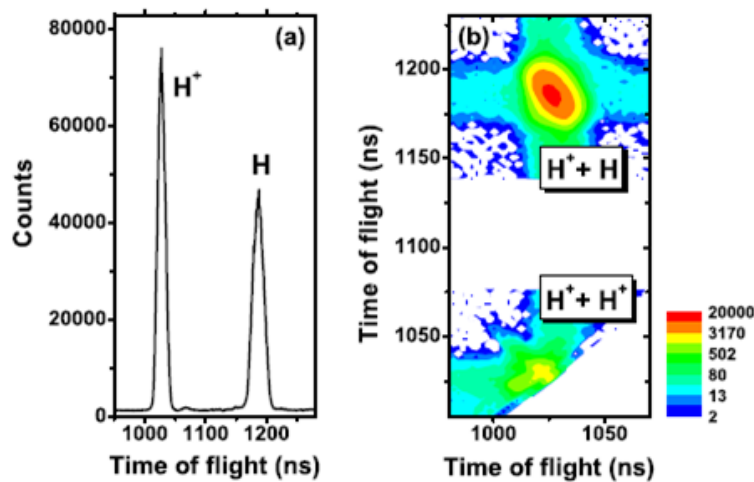
Figure 2.3: (a) TOF spectrum and (b) coincidence TOF spectrum of H_2^+. Note the TOF separation between the ionic and neutral fragments imposed by the spectrometer field (Figure reproduced from [48]).

the interaction between the molecule and the laser are accelerated by a weak electric field parallel to the ion beam toward a detector. The process is sketched in Fig. 2.2. Due to the electric field, different fragmentation channels are separated in the coincidence time-of-flight (TOF) (Fig. 2.3(a)) measurement as shown in Fig. 2.3(b). The impact position and time of those fragments on the detector are recorded. The desired three dimensional momentum distribution can be derived from the recorded position and time of each fragment.

Chapter 3

Theoretical Background

3.1 Major Theoretical Methods

Two methods, i.e. the time-dependent Born-Oppenheimer method (TDBOM) and the time-dependent Floquet-Born-Oppenheimer method (TDFBOM), are used in this thesis to resolve the dynamics of H_2^+ (and its isotopes) dissociation in an ultrashort intense laser field. To give a little more details here, TDBOM is the general time-dependent Schrödinger equation (TDSE) starting with a field-free molecular bound state or superposition of bound states, while TDFBOM is based on Fourier transformation turning the TDSE into an infinite number of coupled equations. The former is actually the most used and the most accurate theoretical method to investigate the dynamics of H_2^+ in a short pulsed laser field, while the latter is usually applied to a long or intermediate pulsed laser field. However, with some special mathematical transformations, the Floquet method can also be used to handle short-pulse cases as elaborated in this chapter and demonstrated in Chapter 5 and 6.

The advantage of the TDBOM is that it is comparatively easy to implement numerically, while the disadvantage is that it cannot explicitly be used to analyze multiphoton processes, where an "energy analysis method" has to be used as a supplement to separate different photon pathways as illustrated in Chapter 6. Conversely, the TDFBOM can explicitly

separate multiphoton processes, in other words, the wavefunction can be expanded onto photon states, while it is a bit of a headache to deal with tens of Floquet blocks to guarantee convergence, especially when the laser peak intensity is high and the pulse length is short.

Both the TDBOM and the TDFBOM utilize the Born-Oppenheimer representation without nuclear rotation and fix the molecular axis along the linearly polarized laser field (1-D model, see following section).

3.1.1 Approximations used in this Thesis

Field-Aligned Model (1-D Model)

Hydrogen molecular ions subjected to a linearly polarized intense laser field have been observed to dissociate preferentially in the direction of the polarization axis [14]. This allowed theorists to discuss the dynamics using one-dimensional models where the diatomic molecule is simplified to be totally aligned in the laser electric field, with its internuclear axis along the polarization axis and the internuclear distance R as the only dissociation coordinate. This phenomenon stems from experimental evidence [49] and later was confirmed by full 3D time-dependent calculations [50]. However, recent theoretical calculations by F. Anis and B. D. Esry [51] show that rotation plays a role in H_2^+ dissociation even if the pulse duration is much shorter than the H_2^+ rotational period ($\approx 556 fs$). For such a short pulse, the different rovibrational states of the molecule are populated but significant rotation only occurs after the pulse and angle-averaged aligned calculation, in which the angle between the internuclear axis and the polarization direction of the laser field is fixed and the final dissociation spectrum is obtained by averaging over the calculations with different angles, gives a very good agreement with the calculation including nuclear rotation [52]. However, as the pulse length become longer, the molecule is more aligned along the field direction during the pulse and the agreement between the two model calculations will worsen, therefore, nuclear rotation must be considered to render closer comparison with experimental observable.
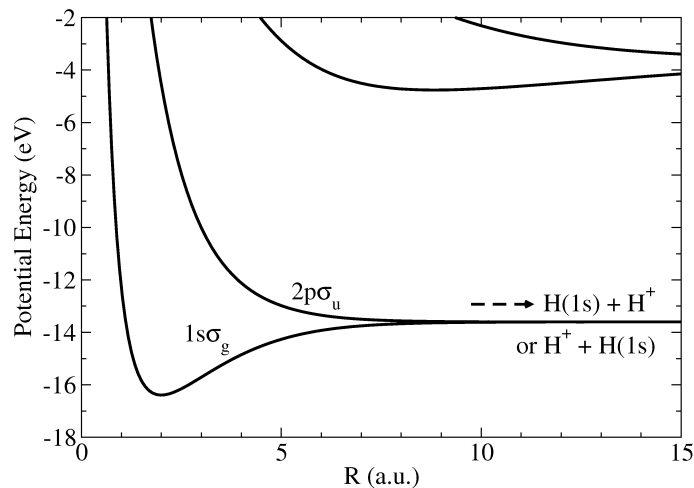
Figure 3.1: Born-Oppenheimer potential curves.

Two-State Model

After adopting the 1D model, the Born-Oppenheimer approximation is then employed to set up a basis to expand the time-dependent wavefunction. The dissociation of H_2^+ in strong laser fields has been mostly described within the two-state model, i.e. the attractive ground state $1s\sigma_g$, and the first repulsive $2p\sigma_u$ state, which both asymptotically dissociate to H(1s) + H^+. These two states are energetically well separated from any other higher states (see Fig. 3.1). Therefore, the molecular basis may be limited to these two states as long as the coupling between them is expressed in the length gauge and the applied laser field is not too high ($\leq 10^{14} W/cm^2$), while two-state velocity-gauge calculation yields unacceptable results [1, 2, 53].

For the purpose of convergence, more electronic states ($n \geq 2$) were included in the calculations, but after checking the contributions from these higher states, it was found that the dissociation probabilities are less than (1%), so we drew the conclusion that the two-state model is valid under the laser conditions involved in this thesis.

3.1.2   Time-dependent Wavefunction and Two Methods for Solving the TDSE

In this thesis, the nuclear dissociation dynamics was modelled using the two-state time-dependent Schrödinger equation (TDSE) in which the complete wave function $\psi(r, R, t)$ is approximated as a superposition of two electronic eigenfunctions $\varphi_g(r, R)$ and $\varphi_u(r, R)$ (σ_g and σ_u) weighted by the corresponding nuclear amplitudes $F_g(R, t)$, $F_u(R, t)$ (referred to as radial functions later in this chapter):

$$\psi(r, R, t) = F_g(R, t)\varphi_g(r, R) + F_u(R, t)\varphi_u(r, R) \tag{3.1}$$

The details of our implementation of the time-dependent Born-Oppenheimer method (TDBOM) for solving the time-dependent Schrödinger equation are given in Ref. [48]. Briefly, the electronic degrees of freedom were expanded on the field-free Born-Oppenheimer states, leaving coupled time-dependent equations in the internuclear distance R:

$$i\frac{\partial}{\partial t}\mathbf{F}(R, t) = \left[-\frac{1}{2\mu}\mathbf{I}\frac{\partial^2}{\partial R^2} + \mathbf{U}(R) - \mathcal{E}(t)\mathbf{D}(R)\right]\mathbf{F}(R, t). \tag{3.2}$$

The matrix $\mathbf{I}$ is the unit matrix, $\mathbf{U}(R)$ is the diagonal matrix of Born-Oppenheimer potentials, μ is the nuclear reduced mass, $\mathbf{D}(R)$ is composed of the electronic dipole transition matrix elements, which, in the present calculations, are just the parallel σ–σ couplings; and $\mathbf{F}(R, t)$ is the column vector containing the radial wave functions in each channel, namely $F_g(R, t)$, $F_u(R, t)$ for the two-state model. Equation 3.2 was solved using a split operator approximation to the short-time evolution operator [54], and the kinetic energy was approximated with a generalized three-point finite differences formula [55].

In addition to the TDBOM, we use another method to solve the TDSE (for Chapter 5 and 6): time-dependent Floquet-Born-Oppenheimer method (TDFBOM), which additionally expands the nuclear wave functions on photon states using a Floquet-like approach

appropriate for laser pulses.

3.1.3   Common Ideas in Both Methods

Before giving the details specific to the TDFBOM, we will discuss what is common to both.

Laser Electric Field

We take the laser's electric field to be

$$\mathcal{E}(t) = \mathcal{E}_0(t)\cos(\omega t + \varphi) \tag{3.3}$$

where ω is the carrier frequency and φ is the carrier-envelope phase. The pulse envelope is $\mathcal{E}_0(t) = \mathcal{E}_0 e^{-(\frac{t}{\tau})^2}$ with pulse length τ related to the FWHM of the intensity envelope by $\tau = \tau_{\mathrm{FWHM}}/\sqrt{2\ln 2}$. The amplitude of the electric field in atomic units is $\mathcal{E}_0 = \sqrt{I/3.51 \times 10^{16}\,\mathrm{W/cm^2}}$ for a pulse with peak intensity I in $\mathrm{W/cm^2}$. Note that the DC component of the pulse is practically zero ($< 10^{-10}\mathcal{E}_0$) for all φ so long as τ_{FWHM} is roughly two cycles or longer [56].

Franck-Condon Averaging

In order to determine whether the effect we predict might be experimentally observable, it is necessary to specify the experimental set-up that we have in mind so that we can carry out appropriate averages. The experimental arrangement we have in mind is described in detail in Sec. 2.4. In that experiment, the H_2^+ was assumed to be produced in an ion source by electron impact ionization, which usually leads to roughly a Franck-Condon distribution of the vibrational states. The coherence of the vibrational states is assumed to be effectively lost due to the distribution of travel times of the molecular ions from the source to the reaction region since the distribution of travel times is much longer than the vibrational period [48]. In other words, the H_2^+ arrives at the interaction region in an incoherent

Franck-Condon vibrational distribution, therefore, in our calculations, each vibrational state is separately propagated until after its interaction with the pulsed laser. Then, an incoherent sum of the desired physical observable over the initial vibrational states weighted by their Franck-Condon factors is performed to construct the final observable for comparison with experiment. We will refer to this procedure as *Franck-Condon averaging* (FCA). Although we will present theoretical calculations for this particular experimental setup, we expect our results will hold generally.

Intensity Averaging

To allow a more direct comparison with experiment, we also averaged over the laser's intensity distribution in the focal volume. In our calculations, we assume that the transverse size of the molecular ion beam is much larger than the laser focal spot size, but much smaller than the Rayleigh length of the laser beam. Since the ion and laser beams intersect at right angles, we can assume the intensity within the laser-molecule interaction volume varies only in the laser's transverse direction, resulting in a two-dimensional averaging [48]:

$$\frac{d\overline{P}(I_0)}{dE} \propto \int_0^{I_0} \frac{dP(I)}{dE} \frac{dI}{I}, \tag{3.4}$$

assuming a Gaussian focal profile. The proportionality constant in the above equation depends only on the laser focal parameters, but is not usually important since experiments do not typically produce absolute measurements. The spectrum for the channel of interest is $dP(I)/dE$ at peak intensity I. The weight factor dI/I in Eq. (3.4) emphasizes the contributions from the lower intensities that occupy larger volumes in the focus. We refer to this process as intensity averaging (IA) in the later chapters. Franck-Condon averaging enhances the contribution from the low-lying vibrational states, while intensity averaging emphasizes the low intensity contribution.

Consideration for the Finite Energy Resolution in a Experiment

Finally, we will also take into account the finite energy resolution, which is a function of kinetic energy release in a real experiment. We thus simply convolve the Franck-Condon and intensity averaged results with a Gaussian resolution function as expressed in Eq. (3.5). We will approximately take the resolution to be ΔE=0.1 eV, which we believe is a typical energy resolution [57].

$$\overline{P}(E_0) = \int_0^{E_0} P(E) e^{-(\frac{E-E_0}{\Delta E})^2} dE, \tag{3.5}$$

Total Dissociation Probability and Kinetic Energy Release

The observables that we focus on are the total dissociation probability and the *kinetic energy release* (KER) spectrum. The *total dissociation probability* (TDP) is calculated by projecting the time-dependent wave function on all of the bound states and subtracting the result from unity. The KER spectrum is calculated by projecting the time-dependent wave function onto energy-normalized nuclear continuum energy eigenstates.

3.1.4 Time-dependent Floquet-Born-Oppenheimer

Since the number of photons exchanged with the laser field is not directly a physical observable, we wanted to try to find a definitive measure of this quantity. One natural approach is to utilize a Floquet method since it explicitly expands on photon channels. Normally, the Floquet representation is considered appropriate only for CW lasers, although it has been adapted to treat pulses in a few cases [58, 59]. We recently derived, however, a version of Floquet that is exact even for short pulses [21, 60].

Our Floquet treatment rewrites the nuclear wave function $\mathbf{F}(R,t)$ as

$$\mathbf{F}(R,t) = \sum_{n=-\infty}^{\infty} e^{in\varphi} e^{-in\omega t} \mathbf{G}_n(R,t). \tag{3.6}$$

Substituting these into (3.2) and equating the coefficients of the linearly independent func-

tions $e^{in\varphi}$ gives

$$i\frac{\partial}{\partial t}\mathbf{G}_n = \left[\left(-\frac{1}{2\mu}\frac{\partial^2}{\partial R^2} - n\omega\right)\mathbf{I} + \mathbf{U}\right]\mathbf{G}_n - \frac{1}{2}\mathbf{D}\mathcal{E}_0(t)\left(\mathbf{G}_{n-1} + \mathbf{G}_{n+1}\right). \qquad (3.7)$$

Any physical observable can be calculated just as for the time-dependent Born-Oppenheimer approach using Eq. (3.6).

In principle, we could have analyzed the nuclear wave functions from the solution of Eq. (3.2) using Eq. (3.6) to extract the functions $\mathbf{G}_n(R,t)$. It was more convenient, however, to simply solve Eq. (3.7) directly. We again used a split operator approximation with generalized finite differences for the kinetic energy operator [54, 55], using the radial grids as described in the following section. At the highest intensities, 56 Floquet blocks distributed roughly symmetrically about the initial $n=0$ state were needed to get the total dissociation probability converged to four digits. Lower intensities did not require so many Floquet blocks. Care was taken to ensure that the Floquet results agreed with the time-dependent Born-Oppenheimer results: the total dissociation probability between the two methods agree to four digits at the highest intensity and to six digits at the lowest intensity.

3.1.5   Numerical Parameters

The numerical methods employed in the thesis are elaborated in Ref. [51, 54, 55]. The three-point finite differences method is implemented in a nonuniform radial grid. To represent the rapid change of the vibrational wavepacket near the classical turning point and the shorter wavelength in the potential well $(1s\sigma_g)$, slightly more than half of the total grid points are used at $R \leq 20$ a.u. At large R, though, a linear grid is used to represent nearly free motion of the molecule. To reduce reflection from the boundary at R_{max}, a sufficiently large grid is adopted in the calculations. No absorbing boundary is applied in the grid. R_{max} is usually not longer than 100 a.u. and the number of grid points is around 3,000–6,000, which is dependent on laser peak intensity and pulse duration used in the calculations, and

the time-step is 0.5 a.u. to get sufficient 4-digit convergence for the slow nuclear dynamics.

Diabatic Picture vs Adiabatic Picture

The Floquet potentials have long been used to describe laser-induced dissociation of H_2^+ into $p+H$ [59]. There are two kinds of Floquet potential curves: diabatic and adiabatic potential curves. In the diabatic picture, the coupling, which is proportional to the laser-field strength and the dipole matrix element between the two molecular states, is not included. It gives off-diagonal elements in the total Hamiltonian (sometimes called dressed Hamiltonian). On the other hand, adiabatic potential curves are obtained by diagonalizing the diabatic potential curves which turns diabatic crossings into avoided crossings. The gap between the avoided crossing is proportional to the applied laser intensity and the order of the crossing [1, 2]. The adiabatic potentials can be used to identify the main physical mechanisms of dissociation described in Sec. 3.2.

Nonadiabatic Picture

It is easy to mistake "diabatic" for "nonadiabatic". Are they the same? The answer is no. Under the Born-Oppenheimer approximation and in the Floquet picture, "nonadiabatic" means any transition between different electronic channels which does not satisfy dipole selection rules. Nonadiabatic effects usually result from very short rise times (a few femtoseconds) of intense laser pulses. Zero-photon dissociation (ZPD) and below threshold dissociation (BTD) belong to this category and will be elaborated in Sec. 3.2.

3.2 Common Terms for Molecular Dissociation and Ionization

There are many mechanisms to interpret the breakup of molecules based on the Floquet picture and the normal numerical integral of the time-dependent Schrödinger equation. To
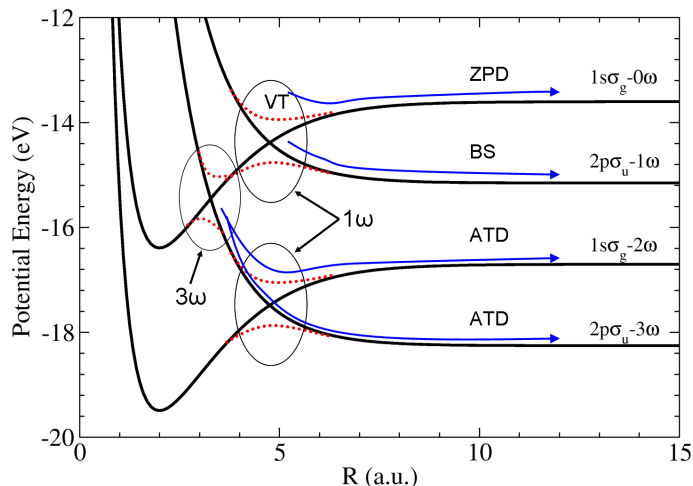
Figure 3.2: Bond-softening (BS), Bond-hardening or Vibrational Trapping (VT), Above Threshold Dissociation (ATD) in Floquet Pictures

name a few here, (see Fig. 3.2), they are bond softening (BS) [47, 61, 62], vibrational trapping (VT) or bond hardening (BH) [47, 62–64], above threshold dissociation (ATD) [1, 2, 65], below threshold dissociation (BTD) [64, 66], zero-photon dissociation (ZPD) [64, 66, 67], charge-resonance enhanced ionization (CREI) [68–72], high harmonic generation [73], and laser-induced alignment [74–76].

Bond softening is a one-photon process in which a molecule's bond "softens" in an intense laser and the molecule comes apart. As Fig. 3.2 shows, the molecule, represented by a wavepacket, passes through the avoided crossing formed between the $1s\sigma_g - 0\omega$ and $2p\sigma_u - 1\omega$ and dissociates along the latter.

Vibrational trapping (VT), also known as bond hardening (BH), is another important one-photon dissociation pathway. Contrary to BS, VT (BH) refers to the reduction in dissociation probability of higher vibrational states due to their trapping in the laser-induced well in the upper dressed Born-Oppenheimer potential curves (Fig. 3.2). This appears as a counterintuitive result since the high-lying vibrational states live longer than expected given their weaker binding.

Above threshold dissociation (ATD) occurs at the three-photon crossings (see Fig. 3.2),

where the molecule absorbs more photons than needed to dissociate. If the wavepacket follows the adiabatic pathway, i.e. $1s\sigma_g - 2\omega$, it will absorb net two photons (absorb three photon and then emit one photon), while if it follows the diabatic pathway, i.e. $2p\sigma_u - 3\omega$, it will absorb three photons.

Below threshold dissociation (BTD) is a nonadiabatic single-photon dissociation mechanism initiated by a photon carrying less energy than the minimum required for the dissociation to occur. It results from the sudden switching on of a strong field so that some vibrational states with energies above the single-photon dissociation threshold are temporarily populated. On the falling stage of the laser pulse, such vibrational states decay to the one-photon channel producing fragments with low velocity and that was referred to as below threshold dissociation (BTD) as opposed to above threshold dissociation (ATD). For H_2^+ and 800nm short laser pulse, net one-photon BTD very likely occurs to $v = 4$ and $v = 5$ states, which are located below the one-photon dissociation threshold $(2p\sigma_u - 1\omega)$ as Fig. 3.2 shows.

Zero-photon dissociation (ZPD) is another important nonadiabatic process in which a molecule dissociates by absorbing net-zero-number photons. This phenomenon is caused by the partial escape of a vibrational wavepacket that is temporarily trapped in a laser-induced well — a signature of vibrational trapping (see Fig. 3.2). For H_2^+ and 800nm short laser pulse, the higher vibrational states $(v \geq 10)$ contribute most to ZPD. ZPD is a special case for below threshold dissociation.

Meanwhile, some new terminologies and new technologies are extending existing nomenclature, like above threshold Coulomb explosion (ATCE) [62, 77], which is a kind of ionization pathway with nuclear kinetic spectra having peaks separated by the photon energy; high order ATD, which reveals an unexpectedly large contribution to ATD from highly excited electronic states [9].

Chapter 4

Isotopic Pulse Length Scaling of H_2^+ Dissociation in an Intense Laser Field

In this chapter, we will demonstrate an interesting isotopic effect that is extracted from the analysis of the dissociation of H_2^+ and its isotope D_2^+ in an intense laser field. By only scaling the pulse durations of the laser exerted on H_2^+ and D_2^+ by the square root of the mass ratio between them ($\sqrt{2}$), similar nuclear kinetic energy release (KER) spectra are produced and after some necessary averaging for comparison with experiment, the resemblance becomes more pronounced. This implies that effectively shorter pulses can be produced by using heavier molecules.

This chapter is based on one of our published paper: [57].

4.1 "$\sqrt{2}$ Effect" and Analysis

Time-dependent Born-Oppenheimer method (TDBOM)(see Chapter 2) is used in this chapter.

It is a well-known and well-used fact that the nuclei in heavier molecules tend to move more slowly than in lighter molecules. This property has been used to "slow down" the
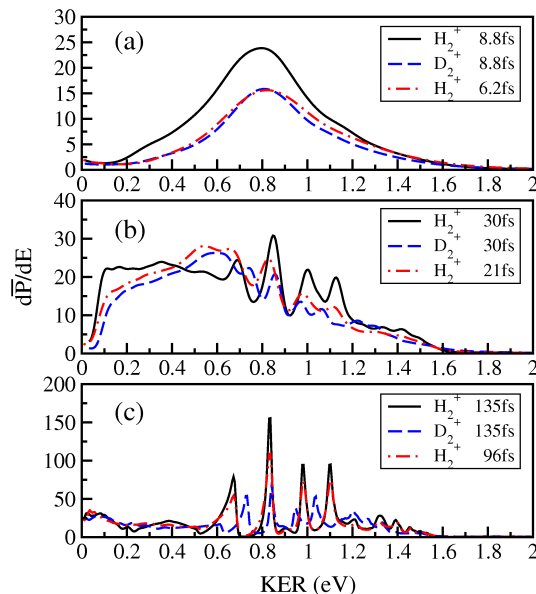
Figure 4.1: $\sqrt{2}$ effect in the nuclear KER spectra of H_2^+ and D_2^+. The pulse wavelength is 800nm; peak intensity is $10^{14}W/cm^2$, and pulse lengths are 8.8/6.2fs, 30/21fs and 135/96fs, for panel (a), (b), and (c), respectively. The KER spectra are after Franck-Condon averaging and intensity averaging for panel (a), (b), and (c).

nuclear motion so that it can be followed dynamically with femtosecond and picosecond laser pulses for many years.

The argument that heavier nuclei move more slowly is based on the fact that at the same kinetic energy, the more massive particles will have the lower velocity. When applied to H_2^+ and D_2^+, this argument suggests that D_2^+ experiences an effectively shorter pulse than H_2^+ [22, 78]. This argument, however, is not typically taken any further than this qualitative observation.

In this chapter, however, we point out the curious result that this argument can lead to nearly quantitative agreement between the KER spectra when applied to H_2^+ and D_2^+. More specifically, we will show that the KER spectra for H_2^+ and D_2^+ nearly coincide for pulse lengths of $\tau/\sqrt{2}$ and τ, respectively. The factor $1/\sqrt{2}$ is the ratio of the H_2^+ relative nuclear velocity to the D_2^+ velocity at the same kinetic energy. In other words, it is simply the square root of the mass ratio of the two species.

Figure 4.1 presents the KER spectra after Franck-Condon and intensity averaging for different pulse lengths. All spectra are for an 800 nm laser pulse with peak intensity 10^{14} W/cm^2. We chose three sets of pulse lengths: short (8.8 fs/6.2 fs), intermediate (30 fs/21 fs) and long (135 fs/96 fs). The ratio of the two pulse lengths in each set is $\sqrt{2}$. Here "short", "intermediate", and "long" refer to their comparison with the typical vibrational periods of the isotopes, which are around 15 fs. In each panel, we show both H$_2^+$ and D$_2^+$ at the same longer pulse length, and in each case the spectra do not match. We also show in each panel the H$_2^+$ spectrum for a pulse length $\sqrt{2}$ shorter. Its similarity to the D$_2^+$ spectrum in Figs. 4.1(a) and (b) is clear.

In Fig. 4.1(a), the 8.8 fs D$_2^+$ spectrum matches the 6.2 fs H$_2^+$ spectrum almost perfectly. The dominant dissociation pathway is bond-softening via a one-photon transition [1, 2, 48] as manifested by the KER peak at 0.8 eV. The 8.8 fs H$_2^+$ spectrum has a similar shape and interpretation as the others, but is uniformly larger. Unless care were taken experimentally to properly normalize these spectra, though, all three would appear to be the same since they share the same shape. The fact that the 8.8 fs H$_2^+$ spectrum is larger can roughly be understood to be the result of the H$_2^+$ travelling faster than D$_2^+$ by a factor of $\sqrt{2}$. More of the H$_2^+$ wavepacket can thus reach the one-photon resonance at $R \approx 4.8$ a.u. in a given time than for D$_2^+$.

As the pulse length becomes longer than the vibrational periods of the two isotopes, more peaks emerge in the KER spectra as displayed in Fig. 4.1(b). Due to the longer pulse length, there is a better chance of resolving the vibrational structure for both species [48]. The peak positions are clearly going to be different for H$_2^+$ and D$_2^+$ since their respective vibrational spectra differ. Due to its heavier mass, the energy gaps between neighboring vibrational states in the ground electronic state of D$_2^+$ are smaller than the ones in H$_2^+$, so the intervals between the peaks are also smaller. Nevertheless, the resemblance of the 30 fs D$_2^+$ and 21 fs H$_2^+$ spectra — and difference from the 30 fs H$_2^+$ spectrum — is clear.

If the pulse length is lengthened to an order of magnitude greater than the vibrational
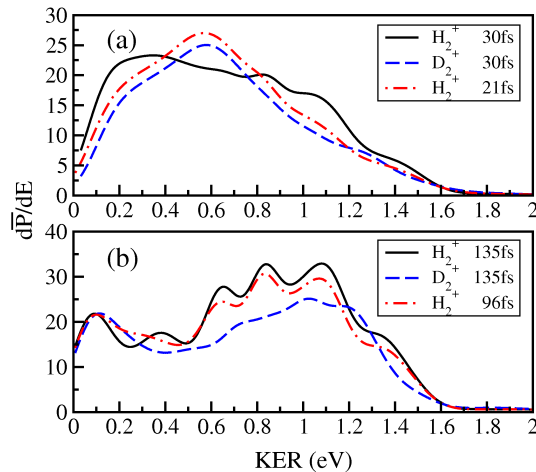
Figure 4.2: $\sqrt{2}$ effect in the nuclear KER spectra of H_2^+ and D_2^+ after Franck-Condon averaging, intensity averaging and convolution. The same laser conditions as in figure 1 are applied.

periods of the two species and beyond, almost all the initial population has the chance to dissociate. The KER spectra are then dominated by the vibrational structure, removing any chance of similarity between the D_2^+ and scaled H_2^+ spectra. Figure 4.1(c) illustrates this case and shows that the 96 fs H_2^+ spectrum is most similar to the 135 fs H_2^+ spectrum not to the 135 fs D_2^+ spectrum.

The domain for which this scaling works can be expanded somewhat when finite experimental resolution is taken into account. Figure 4.2 shows the spectra from Fig. 4.1(b) and (c) for a resolution of 0.1 eV. Figure 4.1(a) is not shown since it is relatively structureless and convolution has little effect. The intermediate pulse length from Fig. 4.1(b), however, retains some vibrational structure, so convolution does have an effect as shown in Fig. 4.2(a). In fact, convolution makes the 30 fs D_2^+ and 21 fs H_2^+ spectra a much better match than in Fig. 4.1. For the long pulses of Fig. 4.1(c) and Fig. 4.2(b), though, convolution is not sufficient to bring the D_2^+ and scaled H_2^+ spectra into agreement.

This pulse length scaling works because H_2^+ and D_2^+ share the same Born-Oppenheimer potential curves and dipole coupling elements. By itself, though, this is not sufficient. The other two contributing factors are the initial distribution of vibrational states and the broad

bandwidth of the laser pulse. Since both species are initially in an incoherent Franck-Condon distribution determined by their respective neutral ground vibrational states, they have essentially the same vibrational state distribution as a function of the vibrational energy. Still, as we have seen, if the pulse length is long, the spectra will simply reflect the vibrational structure. Only when the pulse is short, such that its bandwidth is comparable to the level spacing, will the spectra look similar. For instance, the spacing between the vibrational states nearest the one-photon $1s\sigma_g$–$2p\sigma_u$ resonance is 0.0057 a.u. and 0.0042 a.u. for H_2^+ and D_2^+, respectively. Requiring the bandwidth to be at least half this spacing implies that pulses shorter than roughly 10 fs will yield spectra without vibrational structure. This is a low laser intensity argument that does not take into account any intensity-dependent shifts of the vibrational states which will tend to blur the spectrum even further after intensity averaging. At higher intensities, then, similar spectra can be expected for pulse lengths longer than 10 fs.

4.2   Summary

We have shown that the KER spectra for dissociation of D_2^+ and H_2^+ can be made to match nearly quantitatively for the same peak pulse intensity when the H_2^+ pulse length is $\sqrt{2}$ shorter than the D_2^+ pulse length. We discussed the conditions under which this is true, namely when they have the same broad initial vibrational distribution and are exposed to a short pulse. Under these circumstances, we can use this scaling to produce effectively shorter pulses by using D_2^+. For instance, a 5 fs pulse for D_2^+ would be equivalent to a 3.5 fs pulse for H_2^+.

Although we have used H_2^+ and D_2^+, this pulse length scaling should hold for other molecular isotopes as well so long as they share the same Born-Oppenheimer potentials and dipole matrix elements. The effect for just about any other molecule will be smaller, of course, since the fractional change in mass will be smaller than for H_2^+. On the other hand,

the range of pulse lengths over which the scaling holds will be larger since the vibrational energy spacing of heavier molecules tends to be smaller than for H_2^+.

Chapter 5

The Role of Mass in the Carrier-Envelope Phase Effect for H_2^+ Dissociation

In this chapter, we use the 1-D two-state model to study CEP effects in the dissociation of H_2^+ and its isotopes D_2^+ and T_2^+ in an intense, few-cycle laser pulse, focusing in particular on their differences in order to identify the role of mass. In addition to examining mass's effect on the CEP-dependent asymmetry between dissociation to p+H and H+p along the polarization of the laser electric field, we demonstrate here CEP effects on the *total* dissociation probability. For this observable, we find that the magnitude of the CEP effect grows with mass for the same laser pulse. We further show that the CEP effects in the kinetic energy release (KER) spectra grow with mass from H_2^+ to D_2^+, and from D_2^+ to T_2^+. In both the dissociation asymmetry and the total dissociation, we will show that the recently-developed theory in [21] provides a convenient and insightful description. An alternate, simpler derivation of the latter theory is also provided.

This chapter is based on one of our published paper: [60].

5.1 Simplified Derivation for the General CEP Effect Theory

Time-dependent Floquet-Born-Oppenheimer method (see Chapter 2) is used in this chapter.

A general theoretical framework for understanding CEP effects was recently presented in [21]. At its core, the picture developed there relies on a Floquet representation of the wave function. Consequently, CEP effects are described as interference between different multiphoton pathways. One might be concerned with using the Floquet representation for a laser pulse, but [21] showed that it can be done *exactly* utilizing a two-time (t,t') approach. To set the stage for the discussion in the next section, we rederive the results of [21] here, but will use an alternative approach that some might find more accessible. We note that the present derivation confirms all of the results in [21].

The derivation follows Eq. 3.6 and Eq. 3.7. There are several important features of Eq. 3.7 [21]. First, it is exact — no approximations have been made in the derivation. Second, it is independent of φ. Thus, solving it once is sufficient to generate the full CEP dependence of any observable via Eq.(3.6). Third, since the amplitudes $\mathbf{G}_n$ are associated with the time dependence $e^{-in\omega t}$, they can be interpreted as n-photon amplitudes. Fourth, the only time dependence in the effective Hamiltonian is the relatively slow variation of the pulse envelope.

For the two-state model we will use, one further simplification of Eq.(3.7) is possible. Using the dipole selection rules, the system of equations in Eq.(3.7) can be split into two uncoupled spaces. For instance, the $1s\sigma_g$ state with $n=0$ (zero photons) only couples to the $2p\sigma_u$ states with $n=\pm 1$ and not to the $2p\sigma_u$ state with $n=0$ or the $1s\sigma_g$ states with $n=\pm 1$. The latter three states can thus be treated separately from the former three. Plus, for each n, only a single electronic state is available. We note that the initial state for the present purposes is $1s\sigma_g$ with zero photons.

Finally, while this derivation has been specialized to the present problem of H_2^+, it can

be easily generalized for any problem in the same way as the derivation in [21].

5.2   Results and Discussion

Past studies of CEP effects in molecules have focused on the asymmetry between different dissociation or ionization pathways. In this chapter, however, we will show that even the total dissociation probability — *i.e.* the sum of dissociation probabilities from all possible channels — displays CEP effects. Before we show the numerical results, though, it will be helpful to analyze these physical observables in the framework of the Floquet representation presented in Sec. 5.1.

The most general analysis begins with the atomic channel KER spectra. That is, the spectra for each of the channels p+H and H+p. It is the difference between these channels that gives the asymmetry reported in previous CEP studies [18, 20, 22, 23]. Following the analysis of [1], we label the vibrational continuum eigenstates at energy E in the molecular basis $|gE\rangle$ and $|uE\rangle$ for the $1s\sigma_g$ and $2p\sigma_u$ channels, respectively. The scattering states that we must project onto to find the atomic channel KER spectra are $|Ak\rangle$ and $|Bk\rangle$ where $k^2 = 2\mu E$. The label k reminds us that these must be states that asymptotically become an energy normalized outgoing plane wave, $\sqrt{2\mu/\pi k}e^{ikR}$. Physically, $|Ak\rangle$ corresponds to p+H; and $|Bk\rangle$, to H+p. We can easily calculate $|gE\rangle$ and $|uE\rangle$, from which $|Ak\rangle$ and $|Bk\rangle$ are obtained using

$$|(A,B)k\rangle = \frac{1}{\sqrt{2}}\left(e^{-i\delta_g}|gE\rangle \pm e^{-i\delta_u}|uE\rangle\right) \tag{5.1}$$

where $\delta_{g,u}$ are the energy-dependent scattering phase shifts in each channel. The atomic

channel KER spectra are thus

$$P_{A,B}(E) \equiv |\langle (A,B)k|F\rangle|^2$$

$$= \frac{1}{2}\left| \sum_{n \text{ even}} e^{in\varphi}e^{i\delta_g}\langle gE|F_n\rangle \pm \sum_{n \text{ odd}} e^{in\varphi}e^{i\delta_u}\langle uE|F_n\rangle \right|^2. \tag{5.2}$$

It follows that the total dissociation probability is, after expanding the square and simplifying,

$$P(E) \equiv P_A(E) + P_B(E)$$

$$= \sum_{n \text{ even}} |\langle gE|F_n\rangle|^2 + \sum_{n \text{ odd}} |\langle uE|F_n\rangle|^2$$

$$+ 2\sum_{n \neq n' \text{ even}} \text{Re}\left(e^{i(n-n')\varphi}\langle gE|F_n\rangle\langle gE|F_{n'}\rangle^* \right)$$

$$+ 2\sum_{n \neq n' \text{ odd}} \text{Re}\left(e^{i(n-n')\varphi}\langle uE|F_n\rangle\langle uE|F_{n'}\rangle^* \right), \tag{5.3}$$

while the asymmetry is

$$\mathcal{A}(E) \equiv P_A(E) - P_B(E)$$

$$= 2\sum_{\substack{n \text{ even} \\ n' \text{ odd}}} \text{Re}\left(e^{i(n-n')\varphi}e^{i(\delta_g-\delta_u)}\langle gE|F_n\rangle\langle uE|F_{n'}\rangle^* \right). \tag{5.4}$$

Several important points emerge from these expressions. First, the only CEP dependence is clearly displayed analytically. Second, the CEP dependence of $P(E)$ only has contributions with period π/m, $m=1,2,3,\ldots$ since $n\text{--}n'$ must be an even number in each sum. Conversely, the periodicity of the contributions to $\mathcal{A}(E)$ must be $2\pi/(2m\text{-}1)$, $m=1,2,3,\ldots$. Third, the scattering phase shifts do not contribute to $P(E)$, but do contribute to $\mathcal{A}(E)$. Fourth, to have any CEP dependence in either $P(E)$ or $\mathcal{A}(E)$ requires the amplitudes $\langle (g,u)E|F_n\rangle$ for different photon processes n to contribute at the same energy. It is primarily this

requirement that leads to the need for broad bandwidth, intense laser pulses. For $P(E)$, it is the interference between different photon processes in the *same* molecular channel that is important, but for $\mathcal{A}(E)$, only the interference between different photon processes of *different* molecular channels is important.

One can gain complementary insight by splitting $F_n(R,t)$ into its bound $F_n^B(R,t)$ and continuum $F_n^C(R,t)$ components and writing the integrated total dissociation probability $P=\int dE P(E)$ as

$$P \equiv \sum_n \int dR |F_n^C|^2 + \sum_{n \neq n' \text{ even}} e^{i(n-n')\varphi} \int dR\, F_{n'}^{C*} F_n^C$$
$$+ \sum_{n \neq n' \text{ odd}} e^{i(n-n')\varphi} \int dR\, F_{n'}^{C*} F_n^C. \tag{5.5}$$

These relations, written in the coordinate representation rather than the energy representation, show that P can vary with CEP only if the dissociating wavepackets for different n — but the same electronic state — overlap *spatially*. For H$_2^+$ at moderate intensities, the most likely scenario is that mainly $n=0$, 1, 2, and 3 are populated. Equation (5.5) then predicts that the φ dependence of P should be a linear combination of $\sin 2\varphi$ and $\cos 2\varphi$ on top of a φ-independent background, in agreement with the discussion of Eq.(5.3).

The coordinate and energy representations provide, of course, completely equivalent interpretations of the results. Specifically, the only way for two n-photon channel wavepackets to overlap spatially at $t\to\infty$ is if they have energy components in common by simple kinematic arguments.

Figure 5.1 shows the Franck-Condon averaged P calculated from the solution of Eq.(3.2) for a pulse with peak intensity 10^{14} W/cm^2. From the figure, it is clear that one need not, in principle at least, observe an asymmetry or even a differential quantity to find CEP effects. It is also clear that the main components of P are indeed $\sin 2\varphi$ and $\cos 2\varphi$ as predicted. To facilitate the quantitative comparison of the CEP effect between the isotopes, we define
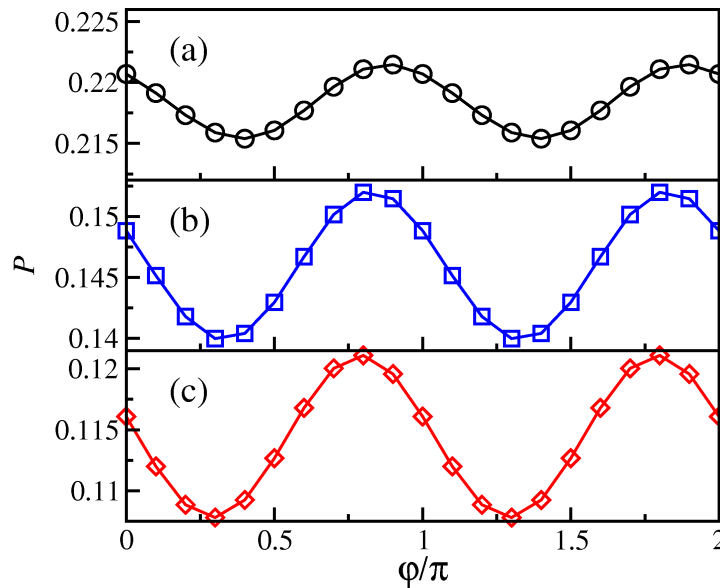
Figure 5.1: The energy-integrated total dissociation probability P (see Eq.(5.5)) in a 5.9 fs, 10^{14} W/cm^2 laser pulse for (a) H$_2^+$, (b) D$_2^+$ and (c) T$_2^+$ with contrasts (see Eq.(5.6)) of 0.0139, 0.0411, and 0.0581, respectively. Note that the vertical scale covers the same range in each panel.

a contrast parameter C,

$$C = \frac{P_{\max} - P_{\min}}{2P_{\mathrm{avg}}},\tag{5.6}$$

where $P_{\max}$ and $P_{\min}$ are the maximum and minimum of P as a function of φ, respectively, and P_{avg} is the average of P over $[0,2\pi]$. By this measure, the CEP effect grows with increasing mass, with more than a factor of 2 jump from H$_2^+$ to D$_2^+$, since C increases from 0.0139 to 0.0411 (0.0581 for T$_2^+$). Interestingly, the contrast for the heaviest isotope, T$_2^+$, increases by only about 50% over D$_2^+$. It is worth noting that even with the intensity averaging required to compare with experiment [48], both the CEP variation and the relative magnitude of the effect survive, giving, for example, $C_{\mathrm{H}_2^+}$=0.0058 and $C_{\mathrm{D}_2^+}$=0.0113 ($C_{\mathrm{T}_2^+}$=0.0154). Convergence testing showed that these results are accurate to four significant digits, giving us confidence that these small CEP effects are real.

A similar trend was seen in [18] where HD^+ was shown to have a larger CEP effect than H_2^+. That comparison was complicated, however, by the fact that HD^+ not only has a larger mass, but also has a permanent dipole moment. We examine only the homonuclear isotopes here to avoid this complication. The dipole couplings are thus identical and any differences must be due to mass.

We expect the CEP effects to become stronger as the peak intensity grows. Since the two-state model employed here neglects ionization, however, we kept the peak intensities below 10^{14} W/cm². Although we could not reliably treat higher intensities, we did check a range of lower peak intensities, from 8×10^9 W/cm² to 10^{14} W/cm², and found that the CEP effects become numerically significant above 5×10^{13} W/cm².

While we have shown that P does vary with the CEP, its small variation makes it a challenge to observe experimentally. Larger CEP effects can be expected, however, for more differential quantities [19, 20], so we show the Franck-Condon averaged $P(E)$ in figure 5.2 under the same laser conditions as for figure 5.1. Each panel is normalized by its overall peak value to emphasize the qualitative differences. The change in the KER spectrum between H_2^+ and T_2^+ is actually rather dramatic. Heavier mass clearly produces a stronger CEP effect. Figure 5.2(d) quantifies this statement with the contrast parameter Eq.(5.6) plotted as a function of KER.

In the context of the Floquet analysis of Eq.(5.3), the figure shows the expected 2φ periodicity, although with an energy-dependent phase shift. Equation (5.3) shows that these phases must come from the amplitudes $\langle (g, u)E|F_n\rangle$ since they contain all of the energy dependence. The vertical yellow stripe common to all isotopes between 0.5 eV and 0.75 eV is the one-photon, bond-softening peak. Since the contribution at these energies is almost entirely from $n=1$, there is little CEP variation. The second vertical red and yellow stripe present in figure 5.2(c) for T_2^+ around 1.7 eV is predominantly three-photon dissociation. The strong CEP variation just above 1 eV is thus due to interference between the one- and three-photon pathways to the $2p\sigma_u$ channel where their amplitudes are comparable and thus
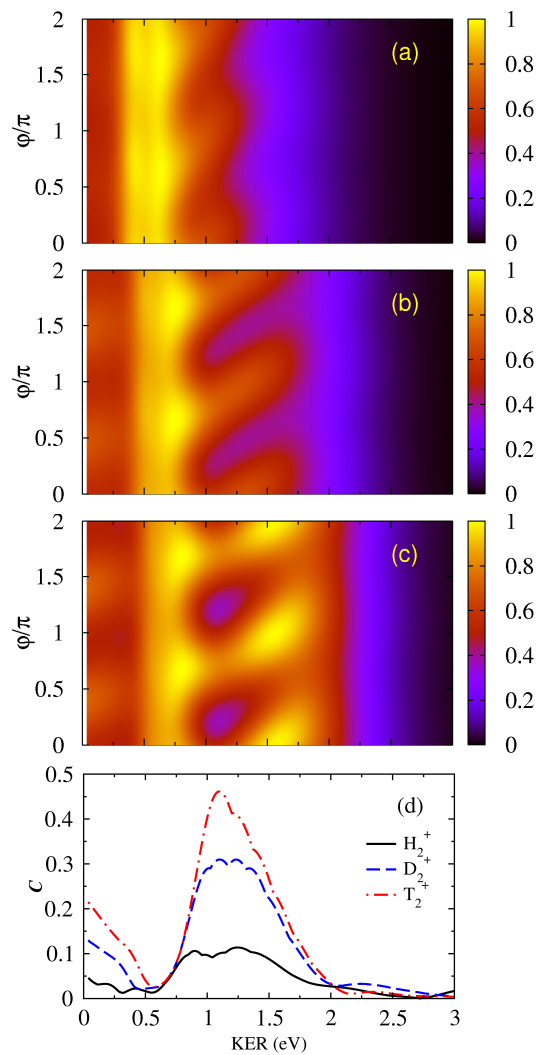
Figure 5.2: The total dissociation probability $P(E)$ as a function of CEP and KER in a 5.9 fs, 10^{14} W/cm^2 laser pulse for (a) H_2^+, (b) D_2^+ and (c) T_2^+. Each panel is normalized to unity at its overall peak value to facilitate qualitative comparison. Panel (d) shows the contrast defined by Eq.(5.6) as a function of KER.
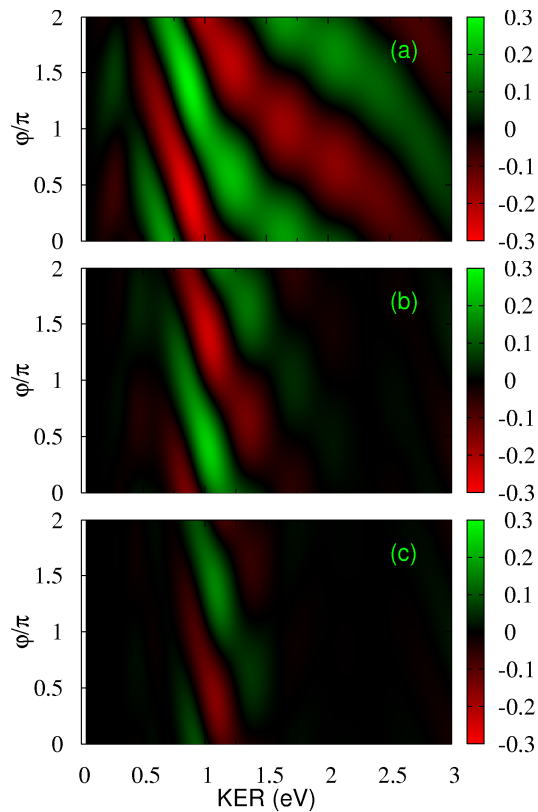
Figure 5.3: The dissociation asymmetry $\mathcal{A}(E)$ as a function of CEP and KER in a 5.9 fs, 10^{14} W/cm^2 laser pulse for (a) H_2^+, (b) D_2^+ and (c) T_2^+. The asymmetry is divided by $2P_{\text{avg}}(E)$ to give a CEP-independent normalization.

produce the highest contrast. Figures 5.2(a) and 5.2(b) show variation in the same energy range due to the same interference, but have a smaller three-photon contribution [9]. The increased CEP variation near zero KER is due to interference between zero- and two-photon dissociation to $1s\sigma_g$.

We complete our discussion of mass's role in the CEP effect with the asymmetry $\mathcal{A}(E)$. Figure 5.3 shows $\mathcal{A}(E)$ normalized at each energy by $2P_{\text{avg}}$. We use this CEP-averaged normalization, which is the same as in Fig. 5.2(d), instead of the more standard $P(E)$ normalization [22] to avoid introducing the CEP dependence of $P(E)$ into the plot. Curiously, increasing the mass *decreases* the CEP effect for the asymmetry — opposite the behavior for the total dissociation probability. The figure does bear out our expectations from the

Floquet analysis (see Eq.(5.4)). Since we expect $n=0$, 1, 2, and 3 to be the primary channels, (see Eq.(5.4)) predicts that the dominant terms should behave as $\cos\varphi$ and $\sin\varphi$ in agreement with the figure. We note that the tilt of the features as a function of energy is opposite to those for $P(E)$. Equations (5.3) and (5.4) make it clear that the energy dependence of $P(E)$ and $\mathcal{A}(E)$ have different origins, however, with the latter depending on the time-independent scattering phase shifts in addition to any laser-induced energy dependence.

5.3 Summary

We have demonstrated both analytically and numerically that there is a CEP effect in the total dissociation probability of H_2^+. The analytical treatment gives considerable insight into the physical processes involved, and the numerical results show that the effect increases with nuclear mass across the isotopes of H_2^+. We further show that under the same laser conditions, the CEP effect previously identified in this system — the asymmetry between breakup channels — decreases with mass. Our analytic expressions reinforce the idea that CEP effects can be understood as interference between different n-photon processes, and show how differential measurements might begin to help us unravel their relative phases.

Chapter 6

Laser–Induced Multiphoton Dissociation Branching Ratios for H_2^+ and D_2^+

In this chapter, we will study the branching ratios for multiphoton dissociation of H_2^+ into p and H. Even though ATD is now a common part of many researchers' intuition, surprisingly little work has been devoted to calculating these branching ratios and quantifying the contributions of one-, two-, and three-photon processes to H_2^+ dissociation — especially for the short pulses now available. Miret-Artés *et al.* calculated branching ratios for a CW laser using a coupled-channel method combined with an artificial-channel technique for a wide range of intensities (from 10^8 to 10^{14} W/cm^2) at 329.7 nm [79]. Yang and DiMauro calculated the branching ratios for various multiphoton processes as a function of intensity, but focused on the narrow range of intensities from 4×10^{12} to 10^{13} W/cm^2 at 532 nm for pulses longer than 100 fs [80]. More recently, Maruyama *et al.* studied the dissociation dynamics of H_2^+ in a 100 fs laser pulse at 800 and 1200 nm, with peak intensities ranging from 10^{12}–10^{14} W/cm^2 using the quasi-stationary Floquet approach [58].

Although people question applying the notion of "photons" to few-cycle laser pulses,

many still interpret the dynamics in terms of multiphoton transitions such as ATD. To investigate whether multiphoton processes can still be identified theoretically and experimentally in these short pulses, we calculate the nuclear kinetic energy release (KER) spectra for H_2^+ and D_2^+ in 5–7.5 fs pulses. At the 800 nm wavelength we use, these are 2–3 cycle pulses and are shorter than the typical vibrational period of either species by roughly a factor of two. We extract the contributions of different multiphoton processes from the KER spectra using two different methods. The first is based solely on the KER; and the second, on the population of Floquet components in the wave function. Only the first method — or the equivalent time-of-flight spectrum — is, of course, available to experiment. We will compare these and discuss to what extent the KER alone can actually be used to determine the number of photons involved. It is important to note that the experimental arrangement we analyze is that of an H_2^+ beam target so that the initial nuclear wave packet is an *incoherent* sum over vibrational states [48] not the *coherent* wave packet appropriate to an experiment starting from neutral H_2.

This chapter is based on one of our submitted paper: [81].

6.1   Laser Conditions and Observables

Time-dependent Born-Oppenheimer method (TDBOM)(see Chapter 2) and time-dependent Floquet-Born-Oppenheimer method (TDFBOM) are used in this chapter.

We carried out calculations for an 800 nm laser pulse with peak intensities ranging from 8×10^9 W/cm^2 to 10^{14} W/cm^2 and pulse lengths from 5 fs to 7.5 fs. At the highest intensities, we tested the convergence with respect to the expansion on electronic states by including all of the states up to those converging to the $n=3$ manifold of H in the separated atom limit. It turned out, though, that all of the states in the $n=2$ and $n=3$ manifolds together contributed less than 1% to the total dissociation probability at 10^{14} W/cm^2. Consequently, we considered no intensities higher than this and included only the $n=1$ states, i.e., $1s\sigma_g$

and $2p\sigma_u$, in the results presented here. This simplification is consistent with our goal of determining whether KER alone is sufficient to identify the probability of different photon processes.

From the total dissociation probability and the KER spectrum, we obtain the multiphoton branching ratios.

6.2 Analysis

Above threshold dissociation was so-named by analogy with above threshold ionization (ATI). In ATI, the photoelectron spectrum typically shows well-defined peaks separated by the photon energy. The peaks can thus be labelled by the number of photons absorbed by the electron with high confidence. Even though the nuclear KER spectrum for dissociation of H_2^+ hardly ever shows clearly separated peaks identifiable with a particular number of photons, different n-photon contributions are still often identified in spectra based on their KER only. As the pulse length gets shorter — and the bandwidth larger — both the ATI and ATD spectra increasingly lose whatever structure they do have, making an energy-based identification of photon number even more difficult. Figure 6.1 shows the calculated KER spectrum for H_2^+ in a 5 fs, 800 nm, 5×10^{13} W/cm^2 laser pulse. It shows one broad peak that cannot obviously be connected to a specific number of photons. Defining the n-photon dissociation probabilities P_n in our non-perturbative calculations is thus the key problem to be solved.

In our Floquet-Born-Oppenheimer representation, the definition is straightforward: P_n is the dissociation probability for a given n-photon channel. The language of the Floquet representation can also be useful, however, for defining P_n from the solutions of Eq. (3.2). The diabatic Floquet potentials, which are the field-free Born-Oppenheimer potentials shifted by integer multiples of ω (in atomic units), are shown in Fig. 6.2. The diabatic potentials can be identified as the diagonal elements of the effective potential matrix in the Floquet-Born-
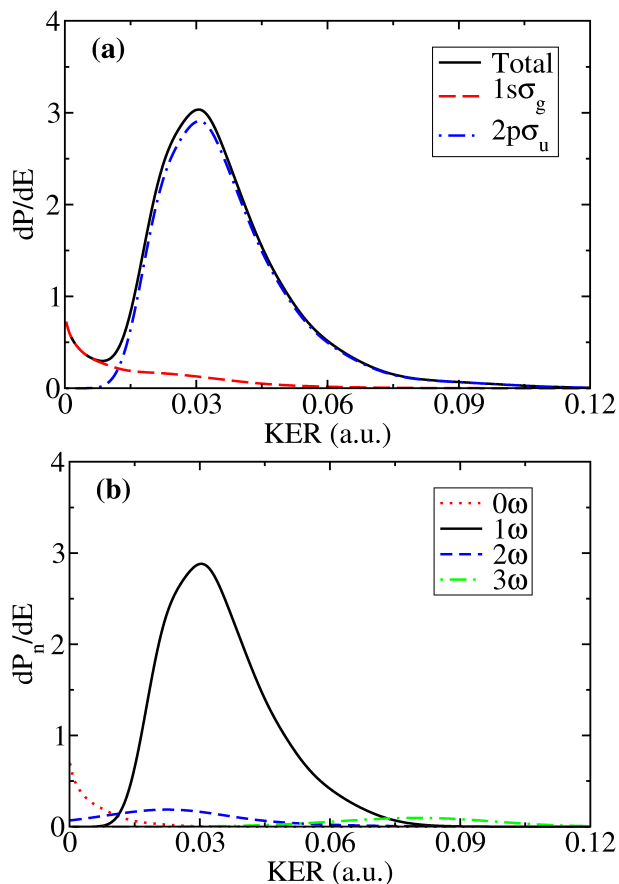
Figure 6.1: (Color online) The Franck-Condon averaged nuclear kinetic energy release spectrum and the contributions from $1s\sigma_g$ and $2p\sigma_u$ for H_2^+ in an 800 nm, 5 fs laser pulse with peak intensity 5×10^{13} W/cm^2 from (a) Born-Oppenheimer and (b) Floquet-Born-Oppenheimer.

Oppenheimer equations (3.7). Also sketched in Fig. 6.2 are the adiabatic Floquet potentials which are obtained from the diabatic potentials by diagonalizing the potential matrix including the dipole coupling due to the laser field. As discussed in Sec. 3.1.1, only the lowest two Born-Oppenheimer potentials, $1s\sigma_g$ and $2p\sigma_u$, are shown since they are sufficient at the intensities considered here. The dynamics of the system can thus be understood in terms of the usual curve-crossing physics familiar from collisions studies.

Figure 6.2 helps us to quickly identify which KER one should expect for n-photon dissociation of a given vibrational level v since energy is approximately conserved in the plot.
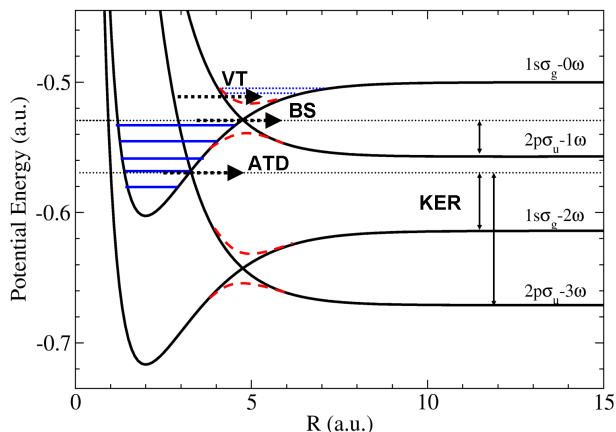
Figure 6.2: (Color online) Diabatic Floquet potential curves for H_2^+ in a linearly polarized 800 nm intense laser field (thick solid lines). The adiabatic Floquet potentials are also sketched (thick dashed line). Different processes are indicated by blue arrows: vibrational trapping (VT), bond-softening (BS), and above threshold dissociation (ATD). The horizontal dotted lines through the $1s\sigma_g - 0\omega \rightarrow 2p\sigma_u - 1\omega$ and $1s\sigma_g - 0\omega \rightarrow 2p\sigma_u - 3\omega$ crossings indicate typical dissociation energy. The KER expected in each case is also shown.

All channels below the initial vibrational energy in the $1s\sigma_g - 0\omega$ curve are energetically accessible making them possible final states. For instance, vibrational states with energies near the crossing between $1s\sigma_g - 0\omega$ and $2p\sigma_u - 1\omega$ will dissociate primarily to $2p\sigma_u - 1\omega$ with a KER given by the difference between the initial vibrational energy and the asymptotic $2p\sigma_u - 1\omega$ threshold. This process is usually called bond-softening. Those vibrational states lying between the $1s\sigma_g - 0\omega \rightarrow 2p\sigma_u - 1\omega$ and $1s\sigma_g - 0\omega \rightarrow 2p\sigma_u - 3\omega$ crossings will dissociate primarily to the $1s\sigma_g - 2\omega$ and $2p\sigma_u - 3\omega$ channels, resulting in ATD. Different initial vibrational states thus lead to different KER ranges for the same n-photon process.

If the laser were on continuously, energy would be strictly conserved in Fig. 6.2. Since we are treating a laser pulse, however, energy is only conserved to within roughly the bandwidth of the pulse. Consequently, vibrational states can dissociate to n-photon thresholds that lie energetically higher via processes generically labelled below threshold dissociation. One way to understand the mechanism producing below threshold dissociation is to imagine the adiabatic Floquet potentials varying in time according to the instantaneous value of

$\mathcal{E}_0(t)$ [59]. In this picture, the gaps at the avoided crossings grow on the leading edge of the laser pulse and shrink on the trailing edge. In particular, the potential well above the $1s\sigma_g - 0\omega \rightarrow 2p\sigma_u - 1\omega$ crossing can trap some part of the vibrational wave function on the leading edge of the pulse. As the intensity grows towards its maximum, the gap grows and the well is lifted. If the intensity is high enough, the well can disappear entirely, depositing anything trapped in it above the dissociation limit of the $1s\sigma_g - 0\omega$ channel. The potential well most efficiently traps the vibrational wave function in short laser pulses since the coupling to it is related to the time-derivative of $\mathcal{E}_0(t)$. Below threshold dissociation thus becomes increasingly enhanced as the pulse length is shortened.

Below threshold dissociation can be understood from Fig. 6.2 by first noting that the gaps at the avoided crossings of adiabatic curves grow with $\mathcal{E}_0(t)$. For instance, parts of the vibrational states lying above the $1s\sigma_g - 0\omega \rightarrow 2p\sigma_u - 1\omega$ crossing become trapped in the adiabatic potential well above the crossing. As $\mathcal{E}_0(t)$ increases, this trapped wavepacket is carried upward with the adiabatic potential. For large enough $\mathcal{E}_0(t)$, the well disappears entirely and the trapped wavepacket dissociates to the $1s\sigma_g - 0\omega$ channel. This particular outcome has received a special name: zero-photon dissociation [64]. This outcome is especially surprising since it represents dissociation with zero net photons absorbed [see, for example, Fig. 6.1(b)].

Since KER spectra like the one in Fig. 6.1 — and similar experimental spectra — do not show a nice comb of peaks separated by ω, information in addition to the energy must be used to define P_n. Unfortunately, this information is only available to theory at this point. Our procedure consists of three basic steps: (*i*) use the dipole selection rules to associate even-number photon processes with $1s\sigma_g$ and odd-number processes with $2p\sigma_u$ and analyze them separately; (*ii*) analyze the spectra originating from different initial vibrational states separately; and (*iii*) apply energy criteria. We will refer to this procedure as the energy analysis method.

The dipole selection rules in our approximation just require that g states only couple

to u states and *vice versa*. With an initial g state, the u state is populated only by odd numbers of photons. Similarly, starting from g, only even numbers of photons can lead to a final g state. If we analyze the KER spectrum for each molecular state separately, then any ATD peaks should be separated by 2ω, making them easier to identify. Figure 6.1 shows the $1s\sigma_g$ and $2p\sigma_u$ KER spectra in addition to the total. Unfortunately, they do not show substantially more structure than the total. The reason is that these spectra have already been averaged over the Franck-Condon distribution of vibrational states (as is appropriate for comparison with experiment).
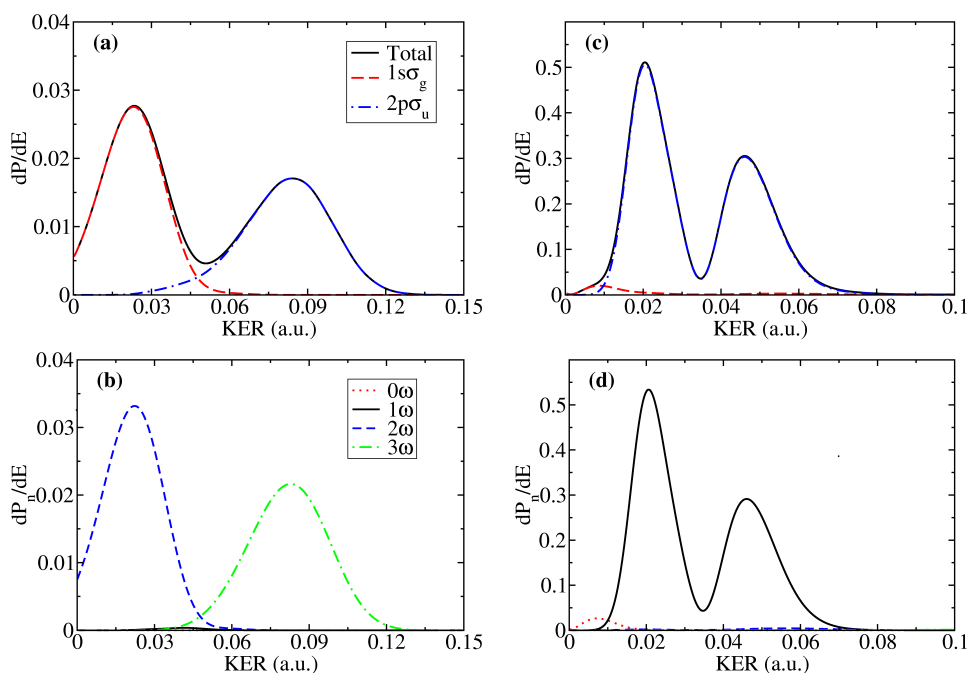
Figure 6.3: (Color online) The nuclear kinetic energy release spectrum for H_2^+ dissociation in an 800 nm, 5 fs laser pulse with peak intensity 5×10^{13} W/cm^2. (a) and (b) are for an initial v=3 state; and (c) and (d), for v=9. In (a) and (c), the Born-Oppenheimer spectra are shown with the individual molecular state contributions; in (b) and (d), the Floquet-Born-Oppenheimer spectra for each photon channel are shown.

To see separate peaks for different photon processes, we must look at the spectra for each initial vibrational state independently. Figure 6.3 shows the KER spectra in both the Born-Oppenheimer and Floquet-Born-Oppenheimer representations for v=3 and 9, respectively,

under the same conditions as Fig. 6.1. The $v=3$ state is the state nearest the $1s\sigma_g - 0\omega \rightarrow 2p\sigma_u - 3\omega$ crossing in Fig. 6.2, and $v=9$ is nearest the $1s\sigma_g - 0\omega \rightarrow 2p\sigma_u - 1\omega$ crossing. Even for this two-cycle laser pulse, the ATD structure is more clearly produced for each individual initial vibrational state than for the Franck-Condon-averaged total KER spectra. The different photon processes can thus be separated by energy if we analyze the KER spectra for each initial vibrational state independently, using the breakdown by molecular state. Note, however, that the 1ω KER spectrum from the Floquet-Born-Oppenheimer calculation in Fig. 6.3(d) shows two quite distinct peaks. This indicate how complicated the nonperturbative mechanism is due to such a ultrashort (broad bandwidth) and intense laser pulse. Without the clear definition of P_n made possible by the Floquet approach, these would almost certainly be labelled different photon processes although they are separated by only about 0.6ω. More generally, the KER spectra for individual initial vibrational states at the highest intensities for these short pulses can still make identifying P_n based on energy a bit ambiguous. Our calculations indicate that the Franck-Condon averaging will help improve the comparison between Born-Oppenheimer and Floquet-Born-Oppenheimer results. The

Table 6.1: Energy Criteria of multiphoton dissociation processes for H_2^+

$1s\sigma_g$		
	$0\ \omega$	$2\ \omega$
$v = 0 - 8$	N/A	$0 \le E \le 0.0875$
$v = 9 - 19$	$0 \le E \le 0.05$	$0.05 \le E \le 0.0875$
$2p\sigma_u$		
	$1\ \omega$	$3\ \omega$
$v = 0 - 4$	N/A	$0 \le E \le 0.116$
$v = 5 - 8$	$0 \le E \le 0.105$	$0.105 \le E \le 0.116$
$v = 9 - 19$	$0 \le E \le 0.105$	$0.105 \le E \le 0.116$

energies used to define different multiphoton processes are given in Tables 6.1 and 6.2. As can be seen in the tables, it was not necessary to define unique ranges for each vibrational state. Rather, we could define energies appropriate for a group of states. To convince ourselves that the choices in the tables were not unreasonably sensitive to our definition,

Table 6.2: Energy Criteria of multiphoton dissociation processes for D_2^+

$1s\sigma_g$		
	$0\,\omega$	$2\,\omega$
$v = 0 - 11$	N/A	$0 \leq E \leq 0.0725$
$v = 12 - 27$	$0 \leq E \leq 0.06$	$0.06 \leq E \leq 0.0725$

$2p\sigma_u$		
	$1\,\omega$	$3\,\omega$
$v = 0 - 5$	N/A	$0 \leq E \leq 0.15$
$v = 6 - 11$	$0 \leq E \leq 0.12$	$0.12 \leq E \leq 0.15$
$v = 12 - 27$	$0 \leq E \leq 0.12$	$0.12 \leq E \leq 0.15$

we varied the energy criteria by $\pm 5\%$ and checked the variation in the resulting P_n. If the relative change in P_n was less than $\pm 1\%$, the energy criteria were deemed acceptable.

Note that in our analysis we only consider zero- to three-photon processes because they account for more than 99% of the total dissociation probability. Our calculations show that the probabilities of these four photo processes are roughly one order of magnitude higher than the contributions of $n \geq 2$ electronic channels. This verifies again that two-state model is valid under the laser conditions used in our calculations. While we do not calculate P_n for higher-order multiphoton processes, their effects are included in the time-dependent calculations. Except for the zero-photon dissociation channel, we do not separately identify below-threshold dissociation in our energy analysis either. Since below-threshold dissociation is initiated from more-or-less the same vibrational states as three-photon ATD and their energy spectra overlap, it is difficult to separate them. For example, vibrational states just below the $2p\sigma_u - 1\omega$ threshold, near the $1s\sigma_g - 0\omega \rightarrow 2p\sigma_u - 3\omega$ crossing, can dissociate to the $2p\sigma_u - 1\omega$ channel via below-threshold dissociation. Their contribution would tend to appear at low KER. The 1ω Floquet spectrum in Fig. 6.1(b) shows very little contribution at low KER, suggesting that below threshold dissociation is negligible for these pulse parameters.

6.3   Results and Discussion

6.3.1   Comparison with Floquet Approach

Before discussing the results of the calculations and analysis, we will show that the two methods for obtaining P_n discussed above do give agreement. More specifically, the less rigorous energy analysis method agrees with the Floquet approach. Since the Born-Oppenheimer calculations are much simpler — two channels rather than tens of channels for Floquet-Born-Oppenheimer — this agreement reduces the computational burden significantly. All of the results in later sections will thus be based on the Born-Oppenheimer calculations combined with the energy analysis described in Sec. 6.2.
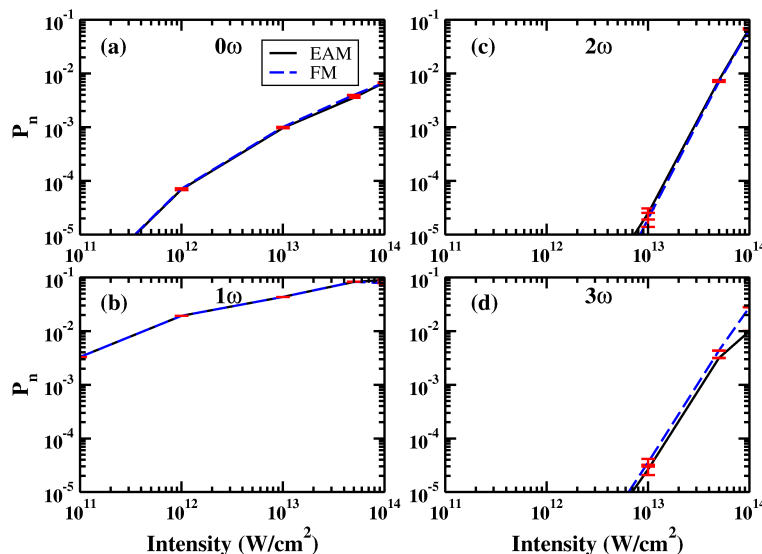
Figure 6.4: (Color online) Comparison of Franck-Condon-averaged multiphoton dissociation probabilities P_n calculated by the energy analysis method (EAM) and the Floquet method (FM) for an 800 nm, 5 fs laser pulse. The error bars, shown in red, indicate the difference in the total dissociation probability from the two methods. Zero, one, two and three photon dissociation probabilities are shown in (a),(b),(c) and (d), respectively.

Figure 6.4 compares the Franck-Condon averaged P_n from the two methods directly as a function of peak intensity for 5 fs, 800 nm laser pulses. Since these were obtained from two distinct calculations, there is some numerical error associated with each. We estimate

this error from the difference in the total dissociation probabilities from the two methods and display it in the figure as the error bars shown for each P_n. Numerical convergence of the two calculations was separately checked with respect to the density of radial grid points, size of the radial grid, and the time step. As stated previously, the total dissociation probabilities thus obtained from the two methods agree to six digits at the lowest intensity and four digits at the highest intensity. Consequently, only differences in P_n larger than these error bars should be regarded as arising from the energy analysis.

From Fig. 6.4, it can be seen that the agreement between the Floquet analysis and the energy analysis is best for the larger channels: 0ω and 1ω. The agreement for the weaker 2ω and 3ω channels is still quite good, and the agreement for all channels degrades with increasing intensity. Based on this agreement, we will only use the energy analysis to define P_n in the remainder of this work.

6.3.2 H_2^+

Figure 6.5 shows the multiphoton dissociation branching ratios as a function of laser pulse length for H_2^+ at two different laser peak intensities: 10^{13} W/cm^2 and 10^{14} W/cm^2. The branching ratios are defined as

$$R_n = \frac{P_n}{\sum_{n'} P_{n'}}, \tag{6.1}$$

where R_n is the branching ratio for an n-photon process. The top row of the figure includes only Franck-Condon averaging, and the bottom row adds intensity averaging. Overall, the figure shows that multiphoton processes are more significant at higher intensity as expected.

Figure 6.5 shows that the 0ω and 3ω branching ratios trend generally downward with increasing pulse length, while the reverse is true for the 1ω and 2ω branching ratios. Since the mechanism for zero-photon dissociation can be thought of as non-adiabatic, it is suppressed as the pulse length grows. Conversely, the adiabatic pathways will grow more dominant in this limit, and the adiabatic pathways lead to the 1ω and 2ω channels. These trends are
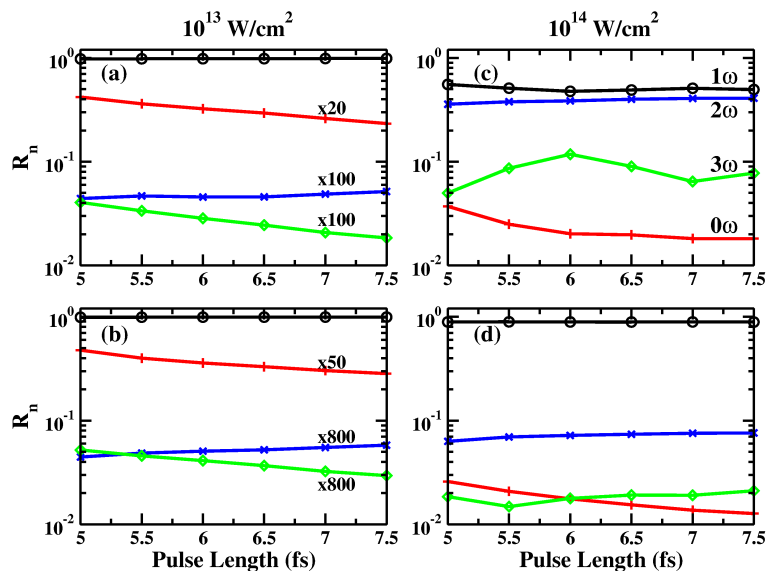
Figure 6.5: (Color online) Multiphoton dissociation branching ratios R_n for H_2^+ at two different peak laser intensities: 10^{13} W/cm^2 (left column) and 10^{14} W/cm^2 (right column). (a) and (c) have been Franck-Condon averaged, while (b) and (d) are also intensity averaged. In the figure, zero, one, two and three photon branching ratios are represented by red pluses, black circles, blue asterisks, and green diamonds, respectively.

thus understandable qualitatively from the common picture of H_2^+ dissociation.

Quantitatively, the overwhelming dominance of the 1ω channel is expected, but the magnitude of the 0ω channel is not. Also a bit surprising is the fact that 0ω goes from the second largest channel to essentially the smallest channel when the intensity is changed from 10^{13} W/cm^2 to 10^{14} W/cm^2. Upon reflection, however, this intensity dependence can be understood by recognizing that the higher intensity pulse is effectively much longer since it spends a longer time at and above the intensities important for vibrational trapping and thus zero photon dissociation [67]. Longer pulses, of course, favor the adiabatic pathways over non-adiabatic ones, suppressing 0ω and 3ω as mentioned above. The suppression of the latter is also shown in the higher intensity results in the figure, supporting this interpretation.

The intensity-averaged results shown in the bottom row of Fig. 6.5 show that the 0ω channel is enhanced relative to the other channels. This is because intensity averaging emphasizes the contributions from lower intensities. Lower-order processes are thus enhanced

by this averaging procedure. Using the perturbative result $P_n \propto I^n$, Fig. 6.4 shows that zero photon dissociation is approximately a one photon process. The 2ω channel, however, requires roughly four photons; and 3ω, three photons. The former sounds counterintuitive, but inspection of the Floquet potentials in Fig. 6.2 shows that a wavepacket must first exit the $1s\sigma_g - 0\omega$ channel via a three-photon transition then undergo an additional one-photon transition back to the $1s\sigma_g - 2\omega$ channel — giving four photons in total. The fact that the 2ω channel is actually higher-order than the 3ω is reflected in the relative enhancement of the 3ω channel in the intensity-averaged panels of Fig. 6.4.
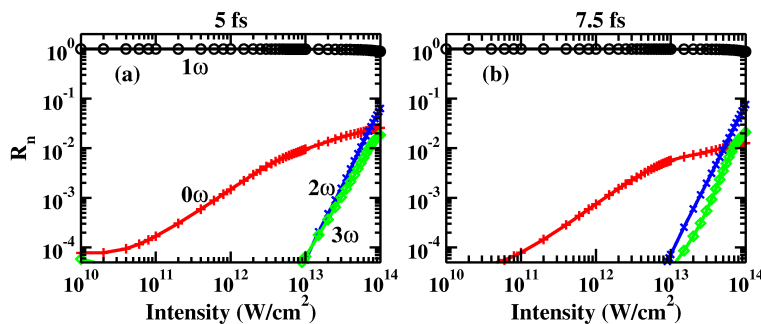
Figure 6.6: (Color online) Multiphoton dissociation branching ratios R_n as a function of the laser peak intensity for H_2^+ in 800 nm, (a) 5 fs and (b) 7.5 fs laser pulses. (a) and (b) have been Franck-Condon averaged and intensity averaged. In the figure, zero, one, two and three photon branching ratios are represented by red plusses, black circles, blue asterisks, and green diamonds, respectively.

Taking another cut through parameter space, Fig. 6.6 shows the intensity dependence of the branching ratios for two different pulse lengths, including Franck-Condon and intensity averaging. As expected, the one-photon process is dominant at all intensities. The zero-photon process is larger than the two- and three-photon processes until about 7×10^{13} W/cm^2, where the two-photon process takes the lead. The branching ratios for both pulse lengths behave essentially the same way as a function of intensity. The most substantial difference is the relative suppression of the 0ω channel in the longer pulse which was discussed above.

6.3.3 D_2^+
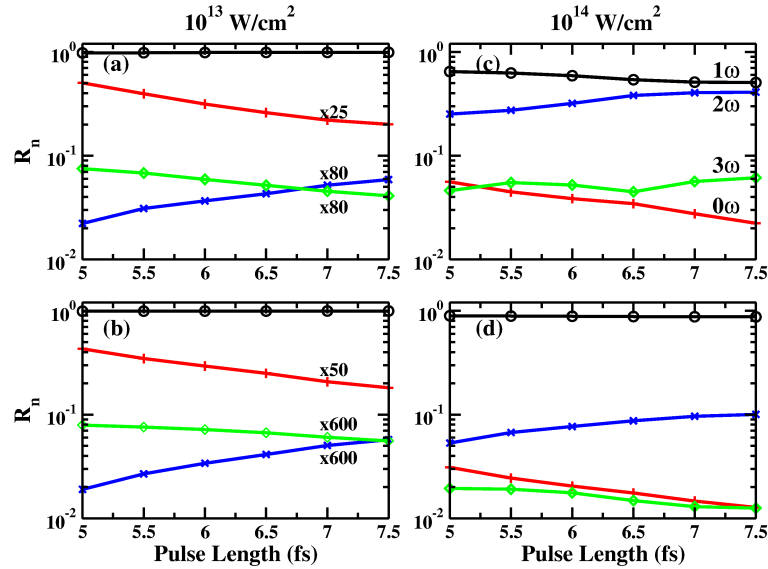
Figure 6.7: (Color online) Multiphoton dissociation branching ratios R_n for D_2^+ at two different peak laser intensities: 10^{13} W/cm^2 (left column) and 10^{14} W/cm^2 (right column). (a) and (c) have been Franck-Condon averaged, while (b) and (d) are also intensity averaged. In the figure, zero, one, two and three photon branching ratios are represented by red plusses, black circles, blue asterisks, and green diamonds, respectively.
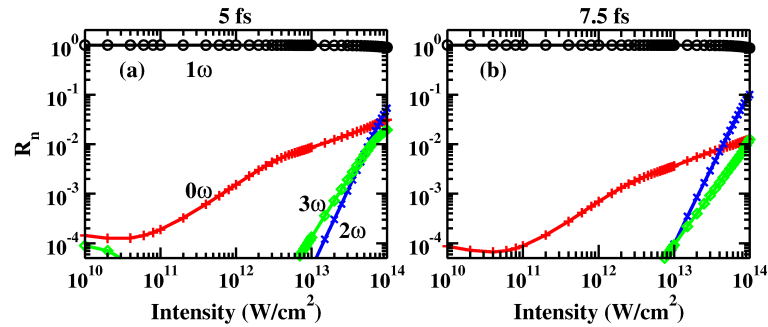
Figure 6.8: (Color online) Multiphoton dissociation branching ratios R_n as a function of the laser peak intensity for D_2^+ in 800 nm, (a) 5 fs and (b) 7.5 fs laser pulses. (a) and (b) have been Franck-Condon averaged and intensity averaged. In the figure, zero, one, two and three photon branching ratios are represented by red plusses, black circles, blue asterisks, and green diamonds, respectively.

To check the effect of nuclear mass on the multiphoton branching ratios, we also cal-

culated R_n for D_2^+. Figure 6.7 shows R_n as a function of the pulse length using the same parameters as for H_2^+ in Fig. 6.5. Any differences from H_2^+ can be assigned to the mass difference which leads to a slower D_2^+ wavepacket — or to an effectively shorter laser pulse [57]. Given the interpretations above based on adiabatic pathways and non-adiabatic transitions, we expect that D_2^+ will show differences from H_2^+. Indeed, the 2ω channel is suppressed relative to H_2^+. The pulse length at which the 3ω channel overtakes the non-adiabatic 0ω channel shifts to larger values for D_2^+ as well, which is also consistent with D_2^+ experiencing an effectively shorter pulse. To complete the comparison, Fig. 6.8 shows the branching ratios as a function of intensity for D_2^+.

6.4 Summary

We have studied the multiphoton dissociation of H_2^+ and D_2^+ in an intense ultrashort laser pulse using the Born-Oppenheimer representation. In particular, we focused on the branching ratios for different n-photon processes, trying to (i) establish a well-defined procedure for identifying them in the KER spectra, (ii) understand their systematic behavior for few-cycle pulses, and (iii) uncover the role of the mass in determining the probability of multiphoton transitions. Since the intensities used in the calculations cover quite a wide range — from 8×10^9 W/cm^2 to 10^{14} W/cm^2 — and the pulse lengths are short (5 fs up to 7.5 fs), this work extends previous studies of the branching ratios.

The behavior of the branching ratios can be understood by utilizing the standard picture of Floquet-Born-Oppenheimer potentials. The essential question to be answered is whether the system should follow the adiabatic pathway. To do so requires the laser pulse to be on when the wavepacket passes through each crossing. The adiabatic pathway is thus favored in longer pulses, and our calculations show that higher peak intensities are equivalent to longer pulses.

The issue of adiabaticity was also the determining factor in understanding the role of

mass for these branching ratios. The heavier mass of the D_2^+ means that the nuclei move more slowly than for H_2^+, pushing their behavior closer to the adiabatic limit in the same laser pulse.

Because the H_2^+ targets available currently have a wide range of vibrational states populated, it is essentially impossible to use only simple energy criteria to identify n-photon peaks in the total KER spectrum. By using additional information available in the calculations and comparing with a Floquet calculation, we validated a scheme appropriate to the commonly-used two-channel Born-Oppenheimer approach. Until experiments can prepare H_2^+ targets in specific vibrational states, however, it is unlikely that a similar scheme can be applied experimentally.

Chapter 7

Conclusions and Vista

In this thesis we present our studies for the dissociation of H_2^+ and its isotopes under an ultrashort intense laser. This one-electron system has been one of the much-studied subjects in the field in the past two or three decades due to its simplicity and importance as a benchmark. The study of H_2^+ holds the hope of being able to extend our understanding of more complex systems where full-degree-of-freedom calculations are beyond present computing capabilities.

7.1 Main Conclusions

The main conclusions can be drawn as follows:

(i) Scaling pulse duration between different isotopes by the square root of their mass ratio can produce similar nuclear kinetic energy release spectra and is a way to produce effective shorter pulses.

(ii) Carrier-envelope phase effects exist not only in the common experimental observable — asymmetry — but also in the total dissociation probability, i.e the total yield from all dissociation channels. Among others, *mass* is a controllable factor to manipulate the CEP effect. Our calculations show that CEP effect in asymmetry decreases with increasing

mass, while increases in the total dissociation probability. We attribute this effects to the interference between different n-photon processes.

(iii)The "energy analysis method" holds for the overall spectra after some necessary averaging due to experimental effects, so that it can be used to separate different multiphoton pathways under the assumption that one can look at individual vibrational states. *Mass* can also be used to control the dissociation pathways: diabatic vs. adiabatic or the extent of adiabaticity. The slower motion of D_2^+ due to its heavier mass than H_2^+, makes its behavior closer to the adiabatic limit under the same laser pulse. Our calculations show that higher peak intensities are equivalent to longer pulses.

7.2   Vista

All the calculations involved in this thesis are limited to the simplest molecular systems H_2^+ and its isotopes D_2^+ and T_2^+. They will be instructive calculations for more complex molecular system so that a general conclusion about the role of mass in the dynamics of intense laser-molecule interactions can be drawn. For example, testing the validity of "$\sqrt{2}$ effects" in heavier molecules like O_2^+ and N_2^+ will further explore the possibility for producing effective shorter pulses ($\leq 5fs$). For the CEP effect, the conclusion reached in Chapter 5 will be more significant if we use the results as a motivation for further exploring the possibility for seeing CEP-effects in larger molecules, which is one of the big goals in the atomic-molecular-optical physics and will facilitate CEP control experiments. For the multiphoton branching ratio calculations, it will be beneficial to use the "*mass*" effect to steer the molecules on different dissociation pathways.

Bibliography

[1] A. Giusti-Suzor, F. H. Mies, L. F. DiMauro, E. Charron, and B. Yang, J. Phys. B **28**, 309 (1995).

[2] J. H. Posthumus, Rep. Prog. Phys. **67**, 623 (2004).

[3] I. Ben-Itzhak, P. Q. Wang, J. F. Xia, A. M. Sayler, M. A. Smith, K. D. Carnes and B. D. Esry, Phys. Rev. Lett. **95**, 073002 (2005).

[4] I. D. Williams, P. McKenna, B. Srigengan, I. M. G. Johnston, W. A. Bryan, J. H. Sanderson, A. El-Zein, T. R. J. Goodworth, W. R. Newell, P. F. Taday and A. J. Langley, J. Phys. B **33**, 2743 (2000).

[5] K. Sandig, H. Figger, and T. Hänsch, Phys. Rev. Lett. **85**, 4876 (2000).

[6] D. Pavicic, A. Kiess, T. W. Hänsch, and H. Figger, Phys. Rev. Lett. **94**, 163002 (2005).

[7] K. C. Kulander, F. H. Mies, and K. J. Schafer, Phys. Rev. A **53**, 2562 (1996).

[8] J. T. Lin and T. F. Jiang, Phys. Rev. A **63**, 013408 (2000).

[9] J. Mckenna, A. M. Sayler, F. Anis, B. Gaire, Nora G. Johnson, E. Parke, J. J. Hua, H. Mashiko, C. M. Nakamura, E. Moon, Z. Chang , K. D. Carnes, B. D. Esry and I. Ben-Itzhak, Phys. Rev. Lett. **100**, 133001 (2008).

[10] J. Ludwig, H. Rottke, and W. Sandner, Phys. Rev. A **56**, 2168 (1997).

[11] A. D. Bandrauk and H. Z. Lu, Phys. Rev. A **73**, 013412 (2006).

[12] A. Rudenko, B. Feuerstein, K. Zrost, V. L. B. de Jesus, T. Ergler, C. Dimopoulou, C. D. Schröter, R. Moshammer and J. Ullrich, J. Phys. B **38**, 487 (2005).

[13] M. Y. Shverdin, D. R. Walker, D. Yavuz, G. Yin, and S. E. Harris, Phys. Rev. Lett. **94**, 033904 (2005).

[14] A. Zavriyev, P. H. Bucksbaum, H. G. Muller, and D. W. Schumacher, Phys. Rev. A **42**, 5500 (1990).

[15] K. Vijayalakshmi, A. Talebpour, T. T. Nguyen-Dang, J. Yang, A. D. Bandrauk and S. L. Chin, Phys. Rev. A **62**, 053408 (2000).

[16] A. Gürtler, F. Robicheaux, W. J. van der Zande, and L. D. Noordam, Phys. Rev. Lett. **92**, 033002 (2004).

[17] G. G. Paulus, F. Grasbon, H. Walther, P. Villoresi, M. Nisoli, S. Stagira, E. Priori and S. De Silvestri, Nature (London) **414**, 182 (2001).

[18] V. Roudnev, B. D. Esry, and I. Ben-Itzhak, Phys. Rev. Lett. **93**, 163601 (2004).

[19] V. Roudnev and B. D. Esry, Phys. Rev. A **71**, 013411 (2005).

[20] V. Roudnev and B. D. Esry, Phys. Rev. A **76**, 023403 (2007).

[21] V. Roudnev and B. D. Esry, Phys. Rev. Lett. **99**, 220406 (2007).

[22] M. F. Kling, Ch. Siedschlag, A. J. Verhoef, J. I. Khan, M. Schultze, Th. Uphues, Y. Ni, M. Uiberacker, M. Drescher, F. Krausz and M. J. J. Vrakking, Science **312**, 246 (2006).

[23] X. M. Tong and C. D. Lin, Phys. Rev. Lett. **98**, 123002 (2007).

[24] A. S. Alnaser, M. Zamkov, X. M. Tong, C. M. Maharjan, P. Ranitovic, C. L. Cocke and I. V. Litvinyuk, Phys. Rev. A **72**, 041402 (2005).

[25] G. L. Kamta and A. D. Bandrauk, Phys. Rev. Lett. **94**, 203003 (2005).

[26] C. P. J. Martiny and L. B. Madsen, Phys. Rev. Lett. **97**, 093001 (2006).

[27] I. Ben-Itzhak, P. Q. Wang, A. M. Sayler, K. D. Carnes, M. Leonard, B. D. Esry, A. S. Alnaser, B. Ulrich, X. M. Tong, I. V. Litvinyuk, C. M. Maharjan, P. Ranitovic, T. Osipov, S. Ghimire, Z. Chang and C. L. Cocke, Phys. Rev. A **78**, 063419 (2008).

[28] F. He, C. Ruiz, and A. Becker, J. Phys. B **41**, 081003 (2008).

[29] F. He, C. Ruiz, and A. Becker, Phys. Rev. Lett. **99**, 083002 (2007).

[30] J. Kane Daniel and Trebino Rick , Opt. Lett. **18**, 823 (1993).

[31] P. O'Shea, M. Kimmel, X. Gu, and R. Trebino, Opt. Expr. **7**, 342 (2000).

[32] P. Gabolde, D. Lee, S. Akturk, and R. Trebino, Opt. Expr. **15**, 242 (2007).

[33] I. A. Walmsley and V. Wong, J. Opt. Soc. Am. B **13**, 2453 (1996).

[34] C. Iaconis and I. Walmsley, Opt. Lett. **23**, 792 (1998).

[35] T. Shuman, I. A. Walmsley, L. Waxer, M. Anderson, C. Iaconis and J. Bromage, Opt. Expr. **5**, 134 (1999).

[36] P. Dietrich, F. Krausz, and P. B. Corkum, Opt. Lett. **25**, 16 (2000).

[37] S. Chelkowski and A. D. Bandrauk, Phys. Rev. A **65**, 061802 (2002).

[38] D. B. Milosevic, G. G. Paulus, and W. Becker, Phys. Rev. Lett. **89**, 153001 (2002).

[39] A. Baltuska and Th. Udem and M. Uiberacker and M. Hentschel and E. Goulielmakis and Ch. Gohle and R. Holzwarth and V. S. Yakovlev and A. Scrinzi and T. W. Hänsch and F. Krausz, Nature **421**, 611 (2003).

[40] D. J. Jones, S. A. Diddams, J. K. Ranka, A. Stentz, R. S. Windeler, J. L. Hall and S. T. Cundiff, Science **288**, 635 (2000).

[41] A. Apolonski, A. Poppe, G. Tempea, Ch. Spielmann, Th. Udem, R. Holzwarth, T. W. Hänsch and F. Krausz, Phys. Rev. Lett. **85**, 740 (2000).

[42] R. Holzwarth, Th. Udem, T. W. Hänsch, J. C. Knight, W. J. Wadsworth and P. St. J. Russell, Phys. Rev. Lett. **85**, 2264 (2000).

[43] U. Morgner, R. Ell, G. Metzler, T. R. Schibli, F. X. Kärtner, J. G. Fujimoto, H. A. Haus and E. P. Ippen, Phys. Rev. Lett. **86**, 5462 (2001).

[44] F. W. Helbing, G. Steinmeyer, U. Keller, R. S. Windeler, J. Stenger and H. R. Telle, Opt. Lett. **27**, 194 (2002).

[45] C. Lemell, X.-M Tong, F. Krausz, and J. Burgdörfer, Phys. Rev. Lett. **90**, 076403 (2003).

[46] P. Dombi, A. Apolonski, Ch. Lemell, G. G. Paulus, M. Kakehata, R. Holzwarth, Th. Udem, K. Torizuka, J. Burgdorfer, T. W. Hasch and F. Krausz, New J. Phys. **6**, 1 (2004).

[47] I. Ben-Itzhak, A. M. Sayler, P. Q. Wang, J. McKenna, B. Gaire, Nora G. Johnson, M. Leonard, E. Parke, K. D. Carnes, F. Anis and B. D. Esry, J. Phys. **88**, 012046 (2007).

[48] P. Q. Wang, A. M. Sayler, K. D. Carnes, J. F. Xia, M. A. Smith, B. D. Esry and I. Ben-Itzhak, Phys. Rev. A **74**, 043411 (2006).

[49] D. T. Strickland, Y. Beaudoin, P. Dietrich and P. B. Corkum, Phys. Rev. Lett. **68**, 2755 (1992).

[50] E. E. Aubanel, J.-M Gauthier and A. D. Bandrauk, Phys. Rev. A **48**, 2145 (1993).

[51] F. Anis and B. D. Esry, Phys. Rev. A **77**, 033416 (2008).

[52] F. Anis, T. Cackowski, and B. D. Esry, J. Phys. B **42**, 091001 (2009).

[53] S. Chelkowski, A. D. Bandrauk, A. Staudte, and P. B. Corkum, Phys. Rev. A **76**, 013405 (2007).

[54] S. C. Cheng and B. D. Esry, Phys. Rev. A **72**, 022704 (2005).

[55] M. W. J. Bromley and B. D. Esry, Phys. Rev. A **69**, 053620 (2004).

[56] D. B. Milosevic, G. G. Paulus, D. Bauer, and W. Becker, J. Phys. B **39**, R203 (2006).

[57] J. J. Hua and B. D. Esry, Phys. Rev. A **78**, 055403 (2008).

[58] I. Maruyama, T. Sako, and K. Yamanouchi, J. Phys. B **37**, 3919 (2004).

[59] S.-I. Chu and D. A. Telnov, Phys. Rep. **390**, 1 (2004).

[60] J. J. Hua and B. D. Esry, J. Phys. B **42**, 085601 (2009).

[61] P. Bucksbaum, A. Zavriyev, H. Muller, and D. W. Schumacher, Phys. Rev. Lett. **64**, 1883 (1990).

[62] B. D. Esry, A. M. Sayler, P. Q. Wang, K. D. Carnes, and I. Ben-Itzhak, Phys. Rev. Lett. **97**, 013003 (2006).

[63] A. Giusti-Suzor and F.H.Mies, Phys. Rev. Lett. **68**, 3869 (1992).

[64] L. Frasinski, J. H. Posthumus, J. Plumridge, and K. Codling, Phys. Rev. Lett. **83**, 3625 (1999).

[65] P. A. Orr, I. D. Williams, J. B. Greenwood, I. C. E. Turcu, W. A. Bryan, J. Pedregosa-Gutierrez and C. W. Walter, Phys. Rev. Lett. **98**, 163001 (2007).

[66] J. H. Posthumus, J. Plumridge, L. J. Frasinski, K. Codling, E. J. Divall, A. J. Langley and P. F. Taday, J. Phys. B **33**, L563 (2000).

[67] L. J. Frasinski, J. Plumridge, J. H. Posthumus, K. Codling, P. F. Taday, E. J. Divall and A. J. Langley, Phys. Rev. Lett. **86**, 2541 (2001).

[68] T. Zuo and A. D. Bandrauk, Phys. Rev. A **52**, R2511 (1995).

[69] T. Seideman, M.Y.Ivanov, and P.B.Corkum, Phys. Rev. Lett. **75**, 2819 (1995).

[70] S. Chelkowski, T. Zuo, O. Atabek, and A. D. Bandrauk, Phys. Rev. A **52**, 2977 (1995).

[71] J. H. Posthumus, L. J. Frasinski, A. J. Giles, and K. Codling, J. Phys. B **28**, L349 (1995).

[72] E. Constant, H. Stapelfeldt, and P.B.Corkum, Phys. Rev. Lett. **76**, 4140 (1996).

[73] T. Zuo, S. Chelkowski, and A. D. Bandrauk, Phys. Rev. A **48**, 3837 (1993).

[74] M. Uhlmann, T. Kunert, and R. Schmidt, Phys. Rev. A **72**, 045402 (2005).

[75] E. Charron, A. Giusti-Suzor, and F.H.Mies, Phys. Rev. A **49**, R641 (1994).

[76] J. H. Posthumus, J Plumridge, M K Thomas, K Codling, L J Frasinski, A J Langley and P F Taday, J. Phys. B **31**, L553 (1998).

[77] B. D. Esry and I. Ben-Itzhak, Private Talk

[78] I. A. Bocharova, H. Mashiko, M. Magrakvelidze, D. Ray, P. Ranitovic, C. L. Cocke and I. V. Litvinyuk, Phys. Rev. A **77**, 053407 (2008).

[79] S. Miret-Artes, O. Atabek, and A. D. Bandrauk, Phys. Rev. A **45**, 8056 (1992).

[80] B. Yang and L. F. DiMauro, Laser Phys. **3**, 398 (1993).

[81] J. J. Hua and B. D. Esry, submitted to PRA (2009).

Publications

J. J. Hua and B. D. Esry, *Laser-induced Multiphoton Dissociation Branching Ratios for H_2^+ and D_2^+*, submitted to Phys. Rev. A and under review

J. J. Hua and B. D. Esry, *The Role of Mass in the Carrier-Envelope Phase Effect for Hydrogen Molecular Ion Dissociation*, J. Phys. B: At. Mol. Opt. Phys. 42, 085601 (2009)

J. J. Hua and B. D. Esry, *Isotopic Pulse Length Scaling of Molecular Dissociation in an Intense Laser Field*, Phys. Rev. A 78, 055403 (2008), selected for the December 2008 issue of Virtual Journal of Ultrafast Science

J. McKenna, A. M. Sayler, F. Anis, B. Gaire, Nora G. Johnson, E. Parke, **J. J. Hua**, H. Mashiko, C. M. Nakamura, E. Moon, Z. Chang, K. D. Carnes, B. D. Esry and I. Ben-Itzhak, *Enhancing High-Order Above Threshold Dissociation of Hydrogen Molecular Ion Beams with Few-Cycle Laser Pulses*, Phys. Rev. Lett. 100, 133001 (2008)